Chapter 4

REMOTE SENSING WATER TEMPERATURE IN PERMAFROST RIVERINE CORRIDORS

Samantha R. Baker[1] and Michael P. Lamb[1]

[1]Division of Geological and Planetary Sciences, California Institute of Technology, Pasadena, CA, USA.

Abstract

Water temperature in rivers and floodplains impacts numerous processes including fisheries, ecosystem health, and geochemical cycling and is of particular concern in Arctic environments with rapidly changing temperatures and thawing permafrost. Remote sensing provides contiguous spatial coverage globally but is an underutilized resource for Arctic rivers and wetlands, which often lack in situ data like temperature gauges. We used the remotely sensed 100 m/pixel Land Surface Temperature dataset from Landsat to investigate water temperature maps of riverine corridors in Alaska. We examined three diverse locations in the Yukon River watershed: a typical anastomosing stretch of the Yukon River, the confluence of the Yukon and Tanana rivers, and the meandering Koyukuk River. We created spatially contiguous, accurate (median error of 0.46°C) water temperature maps for these bodies of water > 210 m in width. We demonstrated how water temperature acts as an indicator for floodplain hydrodynamics. We find that, due to turbulent mixing, river temperature from space accurately captures values at depth. River water temperature can trace the mixing of tributaries tens of km from the confluence and shows connectivity, mixing, and stratification of oxbow lakes. Additionally, the surface temperatures of adjacent thermokarst lakes can differ from each other by 5°C likely indicating disruption from lake thermal stratification by intermittent mixing events. We discuss future applications of remote sensed river water temperature for understanding thermal refuges and stresses on salmon populations, predicting thaw-limited river erosion rates, and guiding in situ sensor placement for hydrologic and geochemical studies of changing permafrost environments.

Plain Language Summary

Water temperature plays a critical role in riverine wetlands environments, particularly in the Arctic, where permafrost thaw, chemical cycling, and fishery populations are of concern. River water temperature is typically measured by gauges placed in the water at key locations, but gauges are scarce in the remote Arctic and do not fully capture the complex distribution of temperature in wetlands environments. We therefore explore using remotely sensed temperature data measured by the Landsat satellites, for which there is

complete global coverage, to create surface water temperature maps for three locations in the Yukon River watershed, the largest river in Alaska. Examining their temperatures in late May just after the ice melts, in August, and in October before the ice freezes, we found that for water bodies with widths >210 m, the Landsat data is typically accurate to <1°C. We highlight several capabilities of these maps, including illustrating wetland hydrodynamic processes and varying controls on river temperature across seasons. We demonstrate that these remotely sensed data can be utilized to fill a critical gap in our study of Arctic riverine environments and are integral to understanding important processes in the Arctic, including ecosystem health, greenhouse gas emission, and river erosion.

1 Introduction

The Arctic and subarctic regions are at the forefront of the Earth's changing climate, with rapid changes happening in river corridors. Arctic amplification is causing this region to experience the highest levels of air temperature warming in the world from anthropogenic effects, up to 4 times that of mean global trends (Burn and Kokelj, 2009; Romanovsky et al., 2010; Post et al., 2019). These changes in air temperatures result in warming inland waters with direct impact on hydrologically interconnected river–wetland systems that include abundant tie channels, sloughs, thermokarst lakes and oxbow lakes with highly variable river connectivity (Smith et al., 2005; Grosse et al., 2013). Numerous small lakes, many adjacent to rivers and in the path of their erosion, create a wetland environment that is rapidly changing, highly water temperature-sensitive, and challenging to monitor. Basic questions are difficult to answer: for example, are there significant variations in water temperature between large river channels and their neighboring sloughs, thermokarst lakes and oxbow lakes?

Warming river floodplain systems influences many processes on the frontlines of Arctic change such as permafrost thaw, river erosion, fisheries, and biogeochemical fluxes. For example, river erosion for some permafrost-bearing banks is accelerating (Geyman et al., 2024), endangering infrastructure and nearby communities, and is controlled primarily by increasing river water temperature (Costard et al., 2003; Douglas et al., 2023). These increased bank erosion rates have a cascading effect on the environment by releasing longfrozen bank material that can contain carbon (Douglas et al., 2022; Lininger and Wohl, 2019) and toxic heavy metals (Miner et al., 2021; Smith et al., 2024).

In addition, river temperature has a major impact on fish. In Alaska, salmon migrate annually from the Pacific Ocean up rivers in the Arctic and subarctic to their breeding grounds, and they are exceptionally temperature sensitive. Salmon have been found to have a preferred water temperature of around 15°C (Eliason et al., 2011). At temperatures above 20–28°C, they do not have enough energy to continue swimming and do not survive the migration (Frechette et al., 2018). Salmon that are under thermal stress may be able to survive by visiting thermal refuges, local regions of anomalously lower water temperature. These thermal refuges include intersections with colder tributaries and confluence plumes, groundwater seeps, pools that are sufficiently stagnant to achieve some thermal stratification, and hyporheic exchange (Bilby, 1984; Ebersole et al., 2003; Torgersen et al., 2012). Despite this, some salmon populations have declined dramatically over the past several decades, causing economic hardships for both the commercial industry and Indigenous subsistence fishers (e.g. Biela et al., 2022).

Water temperature in the Arctic is also a critical component of concerns about geochemical fluxes such as feedback loops with greenhouse gas release from rivers and lakes. Inland waters are significant net sources of CO_2 to the atmosphere from biotic respiration and photosynthesis (Cole et al., 1994, Sobek et al., 2005, Kosten et al., 2010), and Arctic lakes are particularly high emitters of CO_2 and CH_4 due to permafrost thaw (Serikova et al., 2019; Zandt et al., 2020; Zabelina et al., 2021). The controls on the quantity of CO_2 from rivers and lakes are not fully understood, but temperature plays a significant modulating role with higher temperatures leading to greater CO_2 release (Åberg et al., 2007; Kosten et al., 2010; Striegl et al., 2012; Ford et al., 2024). It is therefore necessary to understand the water temperature across Arctic landscapes to better model and predict the release of further greenhouse gases from this environment.

Monitoring water temperature changes in permafrost rivers and their surrounding wetlands has been challenging owing to the immense size and remoteness of the Arctic and subarctic. The primary method of measuring river temperature is with in situ temperature probes placed at river monitoring stations (e.g. Kaushal et al., 2010; Isaak et al., 2012; Wrzesiński and Graf, 2022). While these gauges have been an essential tool in tracking river temperature, they are limited in coverage, as they only measure local water temperature and are typically sparsely placed. Moreover, these gauges tend to be placed along large primary channels and do not capture the diverse web of riverine wetland environments (Krabbenhoft et al., 2022). There are major efforts underway to fill this data gap, including the University of Alaska AKTEMP Water Temperature Database – a database of river temperature records from short-term in situ gauges from across the state. While this dataset expands the quantity and hydrologic diversity of in situ gauges, it is still limited in its coverage.

Thermal remote sensing offers a means to partially fill this data gap. While airborne and drone-based studies can provide high spatial resolution (e.g., <15 cm/pixel), such studies are necessarily limited to small study areas and are difficult to implement in remote areas of the Arctic (e.g., Wawrzyniak et al., 2013; Frechette et al., 2018). In contrast, for the past 40 years, satellites have been providing contiguous spatial coverage of global surface thermal emission, which can be converted to surface water temperature in the Arctic and subarctic. In particular, the Land Surface Temperature (LST) dataset is produced from Landsat 4–9 thermal emission data ranging from 120–60 m/pixel in resolution and dating back to 1982 (Cook et al., 2014; EROS, 2020). While satellite-based remote sensing has commonly been used to measure sea surface temperature (e.g. Prabhakara et al., 1974; Minnett et al., 2019) and large lakes (e.g. Layden et al. 2015; Piccolroaz et al., 2024), it has been used less for rivers.

Important previous work has focused on tropical and temperate settings including using LST or bespoke Landsat-derived surface temperatures to quantify the effects of tributaries on water temperature of the Rhône River (Wawrzyniak et al., 2012) and a stretch of the Ganges River (Das et al., 2022). Additionally, Wang et al. (2025) use the Landsat-derived surface temperature to examine the spatial and temporal variation of water temperature on the Yarlung Tsangpo River. LST also has been used to quantify local anthropogenic effects on river temperature including from the dams on the Yangtze River (Ling et al. 2017; Shi et al., 2021) and thermal pollution from hydroelectric plants in Brazil (Alcântara et al., 2010) and France (Wawrzyniak et al., 2012). LST has recently been applied to quantify the decadal-scale warming trends in stretches of the Ganges (Kachari et al., 2024) and Amazon (Santos Fleischmann et al., 2025) rivers. One of the few studies in permafrost terrains to use LST was a validation of the method against an in situ USGS gauge at Pilot Station by Baughman and Conaway (2021), who found mean error of 0.47°C, demonstrating that seasonal trends should be readily measurable.

Here we present an exploratory study to use the LST data to examine spatial and temporal patterns of river and wetland surface water temperature and connectivity at three example study sites along the Yukon River in Alaska. Taking this approach to the Arctic and subarctic poses additional considerations due to extreme seasonality, the complexity of river-wetland systems, and their hydrological connectivity (e.g., Farquharson et al., 2016). Previous studies of remote sensing water temperature have not examined the relationship between river temperature and that of floodplain wetlands, but this holistic view is important in a thermokarst landscape. We have some, but limited, in situ data at these study locations. Here, we do not provide a complete hydrological study of rivers and wetlands, nor do we attempt to test hydrological or thermal models. Instead, as one of the first applications of LST to permafrost river corridors, we demonstrate how remote sensing can be used to generate accurate and spatially continuous seasonal water temperature maps for Arctic wetlands environments, revealing a rich pattern of hydrological connectivity across these dynamic environments.

2 Study Location and Methods

2.1 Study locations

We use the LST dataset to examine how water temperature varies spatially and seasonally in permafrost river corridors. We selected three example locations to span diverse hydrologic contexts along the Yukon River watershed in discontinuous permafrost where change is currently rapid. We examined the meandering Koyukuk River, a major tributary of the Yukon River, near the village of Huslia; the confluence of the Yukon River and the Tanana River near Tanana town; and the anastomosing Yukon River near Beaver, AK (Table 1; Figure 1).

Name	Center coordinates	Description

Huslia	65.76°N, -156.36°E	Single-threaded meandering stretch of the Koyukuk River, a major tributary of the Yukon River
Tanana town	65.18°N, -152.63°E	Intersection of the multi-threaded Yukon River and the Tanana River
Beaver	66.345°N, -147.40°E	Multi-threaded anastomosing stretch of the Yukon River midway along its length, representative of much of the river

Table 1: Descriptions of study locations.

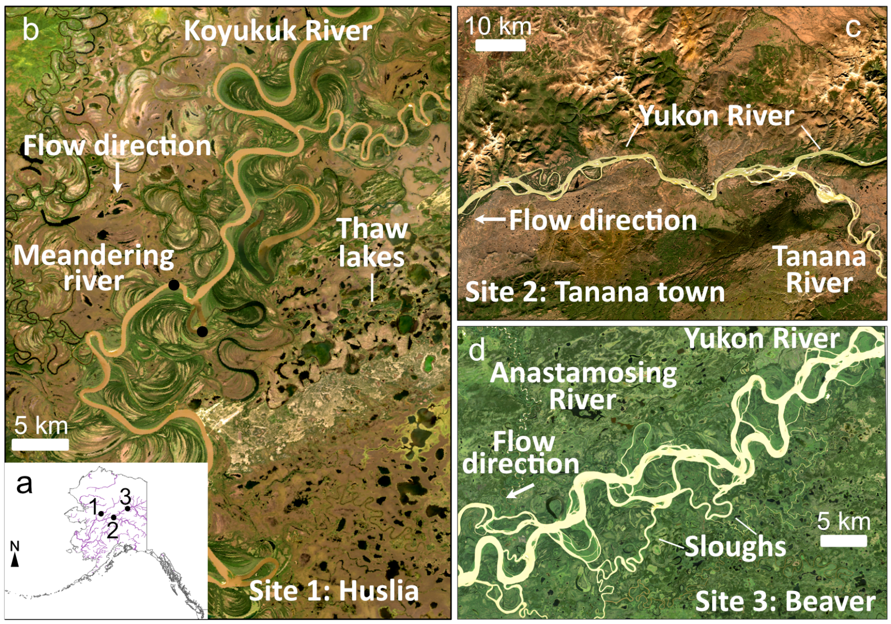

Figure 1: a) Study locations in the Yukon River watershed shown on an outline of the state of Alaska. b–d) Landsat enhanced color visible RGB images of each study location. For each site, some types of fluvial geometry are listed (e.g., meandering, anastomosing), key hydrologic features are identified, and the flow direction of the river is indicated. North is up for all panels. The two black dots indicate the locations of in situ water temperature loggers.

2.2 Landsat derived temperature data

The remote sensing data in this project comes from Landsat 8 Operational Land Imager (OLI) level 2 data products. We used visible–near-infrared (VNIR) reflectance products that were generated with the Land Surface Reflectance Code (LaSRC) algorithm (Vermote et al., 2018) and the Land Surface Temperature data products generated from infrared thermal emission measurements (Cook et al., 2014). Surface temperature data were derived from the thermal emission band. For Landsat 4, 5, and 7, this is one band from 10.40 - 12.50 µm. For Landsat 8 and 9, there are two thermal emission bands at 10.60 - 11.19 µm and 11.50 - 12.51 µm. The amount of energy emitted from a surface at a given wavelength is dependent on its temperature and its emissivity, which is the ratio of energy that is absorbed and re-emitted to the energy that is instead reflected at that wavelength. The emissivity therefore describes the deviation of the material from a perfect blackbody, where all light is emitted, and so the emissivity is equal to 1. This relationship is described by the Stefan-Boltzmann equation:

$$T = \frac{hc}{\lambda k_B \ln\left(\frac{2hc^2}{B\lambda^5}+1\right)\varepsilon} \tag{1}$$

where *h* is Planck's constant, *c* is the speed of light, λ is the wavelength considered, k_B is the Boltzmann constant, *B* is the radiance at the given wavelength (this is the thermal emission measured by Landsat), and ε is the emissivity.

The derivation of temperature from radiance to create the LST dataset is based on this physics with further correction and processing. The effects of atmospheric radiance and scattering are removed as described by Barsi et al. (2014) and Cook et al. (2014). Because Landsat measures only the thermal emission, the surface emissivity must also be known for temperature to be derived (equation 1). Mean monthly emissivity for each pixel was calculated from the Advanced Spaceborne Thermal Emission and Reflectance radiometer (ASTER) multi-band thermal emission data combined with normalized difference vegetation index (NDVI) measurements from the contemporaneous visible–near-infrared Landsat spectral bands as described by Hulley et al. (2012). We find that water is consistently assigned an emissivity of 0.9904. This method of temperature retrieval measures the temperature of approximately the top 10 cm of the water (Handcock et al., 2012).

2.3 Creation of water-only masks for temperature-mapping

For each location of interest, we identified several cloud-free scenes from Landsat 8 across the unfrozen season. We chose an image in May soon after ice breakup, one in August, and one in October before river freezing. We selected only Landsat 8 images to remove any complications that could be introduced by comparing data across Landsat instruments that vary in resolution. The thermal data used for the location of interest maps have a resolution of 100 m/pixel. Landsat 8 began data collection in 2013, and it has an imaging repeat rate of around 2 weeks. This means that any given location has been imaged approximately 350 times by this instrument. To compare images equally and remove the possibility of clouds and cloud shadow affecting or obscuring temperature patterns, we hand-selected only images that completely lacked cloud cover in the area of interest. Because Alaska is a cloudy region, this reduced the number of usable images available for a given season in each location to typically <5. We therefore were limited in clean data availability and so selected a single image for each season that demonstrates the pattern of water temperature across the environment at that time.

For each image, we created a water mask using the method described by Zou et al. (2018) using OLI's visible–near-infrared reflectance bands and the quality assessment band. To be considered water, a pixel must meet the following criteria:

1. Free of cloud cover as defined by Landsat's quality assessment
2. Modified Normalized Difference Water Index (mNDWI) > Enhanced Vegetation Index (EVI) or Normalized Difference Vegetation Index (NDVI)
3. EVI < 0.1

The definitions of NDVI, mNDWI and EVI are:

$$\mathrm{NDVI} = \frac{R_{\mathrm{near-infrared}} - R_{\mathrm{red}}}{R_{\mathrm{near-infrared}} + R_{\mathrm{red}}}$$

(2a)

$$\mathrm{mNDWI} = \frac{\mathrm{R_{green}} - \mathrm{R_{shortwave\ infrared}}}{\mathrm{R_{green}} + \mathrm{R_{shortwave\ infrared}}}$$

(2b)

$$\mathrm{EVI\ (for\ Landsat\ 8)} = \frac{2.5(\mathrm{R_{near-infrared}} - \mathrm{R_{red}})}{\mathrm{R_{near-infrared}} + 6(\mathrm{R_{shortwave\ infrared}}) - 7.5(\mathrm{R_{blue}}) + 1}$$

(2c)

where R_x is the reflectance in the x band (e.g., $\mathrm{R_{green}}$ is the reflectance in the green band). We also masked out some remaining snow by hand.

We use this water mask to isolate the temperature data to only the water temperature in the scene. We examined each generated temperature map to exclude those with obvious artifacts such as stripes across the image. Once we identified artifact-free images for each site of interest, we examined these maps by hand to identify qualitative patterns in water temperature across these diverse riverine environments.

An important limitation on the utility of this dataset for generating spatially resolved temperature maps is the disparity between the available resolution of the LST images and the inherent resolution of the Landsat thermal bands. While Landsat 8 thermal band has a resolution of 100 m, all processed LST data has been resampled to 30 m/pixel using a nearest-neighbor interpolation to match the resolution of the Landsat VNIR bands (USGS, 2025). Therefore, while the water masking is accurate to 30 m/pixel, the temperature values that match each masked water pixel do not necessarily correspond to entirely water because the calculation of its temperature value could have included interpolation from surrounding land temperature.

This trend is evident from the raw masked temperature images where there appears to be a clear cross-sectional variation in river temperature (Figure 2). This is not reflective of the reality of the water temperature, as these rivers are fully turbulent, and therefore temperature is well-mixed across their profile (e.g. Villamizar et al., 2014).

Land and water temperatures can vary substantially due to thermal stratification of the water, how water is sourced from far-reaching environments, and their differing material properties such as specific heat. Because water has a higher thermal inertia than land (i.e., vegetation, rock, and soil), the water in Alaska is colder than the surrounding land in the spring. In the fall, this trend reverses, as water cools more slowly and therefore remains warmer than the land.

To correct for this, we processed the masked LST images to remove 3 pixels from all water edges, as these pixels could have substantial mixing with the land temperature signal. These processed images do not demonstrate this same cross-sectional trend (Figure 2). The necessity for this step limits the size of water features that can be examined with this method. These results suggest that water features must be at least 7 Landsat VNIR pixels (that is, 210 m) across to achieve an accurate temperature signal. Therefore, the method described here of generating spatially resolved water temperature maps can only be applied to especially wide rivers as well as larger ponds.

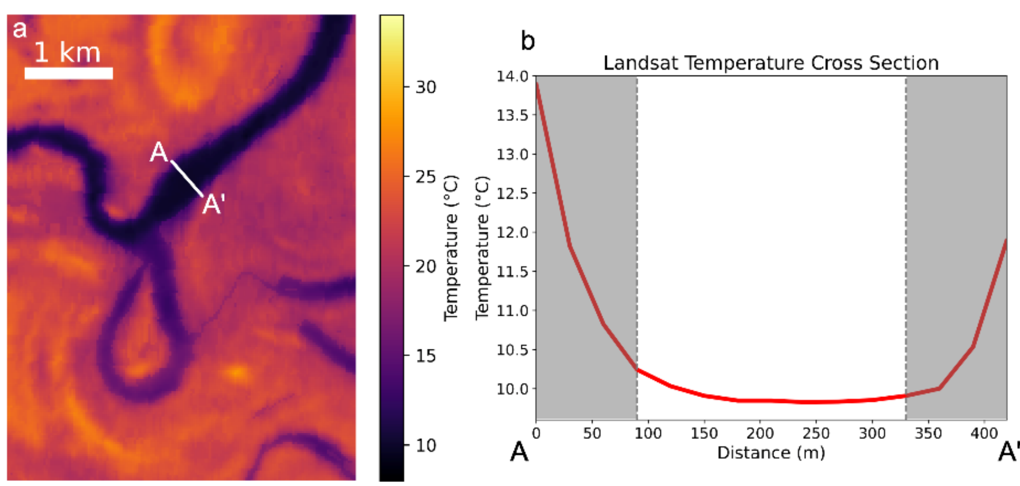

Figure 2: a) Temperature map of a short stretch of the Koyukuk River showing both the ground and water temperature. b) The temperature profile of the segment identified as water in the cross-section. The gray shaded regions indicate the temperature values of the pixels removed from the water temperature maps due to mixing with the land temperature signal.

For all following temperature maps, we show both the masked water temperature and the full water extent. The pixels within the filtered water mask, those for which we are confident the LST dataset is providing the temperature of water with no land signal, are assigned a temperature value and a color based on that map's color scale. These data are plotted on top of a binary map of our full 30 m/pixel water mask generated from Landsat TM bands as described above. This binary map is plotted in black and white, and it demonstrates the full extent of the water in the image detectable by Landsat to provide context to the distribution of water in the scene.

Additionally, the temperatures maps for each region are plotted with two colorbars. For the first, all images are plotted with the colorbar scaled to 0–17°C. This demonstrates at a glance the absolute change in temperature of a location across seasons. For the second, each temperature map is plotted with a divergent colorbar where the middle (white) is centered on the mean water temperature in the visible extent, and the scale limits are ±5°C from that mean. The values plotted in both versions of each map are temperature, but the divergent scale better illustrates the relative temperature variation within a scene.

2.4 Comparison to other data

To ground truth the data, Baughman and Conaway (2021) performed a comparison between the LST temperature and in situ temperature measured at the USGS Pilot Station monitoring station on the Yukon River, and they found that the LST dataset is accurate with a mean difference of -0.47°C (LST temperature – in situ temperature). We corroborated these measurements by comparing the LST temperature values to water temperature measured in situ by the USGS Pilot Station gauge on the Yukon River. We defined a region of interest of approximately 3 km^2 of the Yukon River (Figure 3a) around the location of the gauge and calculated the mean surface water temperature for all available cloud-free Landsat 7, 8, and 9 images (though we only use Landsat 8 for our analysis, we use all available Landsat images for the validation). Landsat 7 launched in 1999, followed by Landsat 8 in 2013 and Landsat 9 in 2021. The thermal infrared bands have spatial resolutions of 60 m for Landsat 7 and 100 m for Landsat 8 and 9.

These images were all taken at around 2 PM local time, so we compared these remotely sensed temperature values to the contemporaneous 2 PM Pilot Station measurements (Figure 3b). We extracted all images of this region of interest with cloud cover <50% across the whole image as measured by the Landsat quality assurance parameter. This resulted in a dataset of 241 images. Many of these images still had cloud cover across the location of Pilot Station, and we removed all these images from the ground truth comparison. This created a cloud-free dataset of 57 images.

To better understand the vertical temperature structure of rivers and oxbow lakes, we also compared the surface water temperature measured by LST to in situ temperature measurements taken at several representative locations. We installed HOBO water level U20L-02 loggers at depth in the main channel of the Koyukuk River and in an oxbow lake near Huslia. These locations are shown in Figure 1. The reported temperature uncertainty for these loggers is ±0.44°C, and they recorded water temperature every 15 minutes throughout the 2023 unfrozen season from May 23 to October 4. We compared the remotely sensed surface temperature to the temperature at depth in the river channel and oxbow lake.

To inform our interpretations of the controls of river temperature in these environments, we also compared the remotely sensed water temperature to local air temperature measurements and the available river discharge measurements. Near surface air temperature was extracted from thermometers located at airports adjacent to each study location. For Huslia, data were taken from Huslia Airport (station 70365526552), for Beaver, Fort Yukon Airport (station 70194026413), and for the confluence, Ralph M Calhoun Memorial Airport (station 70178026529). River discharge measurements are confined to only a few locations where there are in situ discharge gauges, so we used data from the USGS Pilot Station on the Yukon River (Gauge #15565447) as a reference value. Because of the distance between Pilot Station and the study locations, these data do not reflect the absolute discharge at the locations of interest but are instead representative of the relative changes in discharge over the course of the season.

3 Results

3.1 Ground truthing and error assessment

We performed ground truthing of the LST dataset by comparing its temperature values to in situ temperature measurements from the USGS Pilot Station gauge (Figure 3). We define the offset of the LST as the difference between the LST temperature and the contemporaneous Pilot Station in situ temperature. We find LST is very accurate compared to in situ measurements (Figure 3b). Both the mean and median offset of the LST dataset are 0.45°C with a standard deviation of 1.89°C. There are two substantial outliers in this data set with offsets of 6.2°C and 8.7°C. One outlier is caused by optically thin clouds that we were unable to effectively mask out, and the cause of the other is unclear. Excluding these outlier points, the mean offset becomes 0.73°C with a median of 0.46°C and a standard deviation of 1.17°C. We will use these values for this study. The absolute values of these offsets are very similar to those calculated by Baughman and Conaway (2021), who found a mean difference of 0.47°C. However, they found a negative bias in the LST data (i.e., LST values tend to be colder than the in situ values), whereas we find a positive bias. This is likely due to a combination of small differences in method of temperature comparison such as the boundaries of the region of interest and our incorporation of several more years of data, including Landsat 9. We note that these offsets are substantially smaller than typical values given by the accompanying LST uncertainty estimate (ST_QA band), which is calculated from atmospheric correction uncertainties and distance of a pixel to the nearest cloud.

The source of the small offset residual is unclear, but Hulley et al., (2012) have found that the largest source of error in the calculation of LST is air humidity, which affects the atmospheric correction. This variable is approximately constant across the short stretches of river considered here, so the accuracy of the relative temperature within an image is higher than the accuracy of the absolute temperature.

We do not expect water turbidity to be a source of systematic error in the LST measurements (Wen-Yao et al., 1987; Wei et al., 2017). While turbidity can affect water's emissivity and therefore the calculation of temperature from thermal emission measurements, Wen-Yao et al. (1987) found that significant deviations in water emissivity only begin to occur at sediment concentrations of 10^4–10^5 mg/L, and the largest turbidity found in Alaskan rivers is around 1000 mg/L (Chikita et al., 2002) and is usually much less than that (Brabets and Ourso, 2013). Similarly, Wei et al. (2017) model the effects of turbidity on emissivity for application to remote sensing of sea surface temperature, and they found that turbidity has a negligible effect (0.2°C) for sediment concentrations smaller than 1000 mg/L. We corroborated this finding by comparing the temperature difference between in situ and remotely sensed temperature to the near-infrared albedo (0.85 - 0.88 μm), which acts as a proxy for turbidity (e.g. Wu et al., 2014; Hossain et al., 2021). We show the results of that comparison in Figure 3c, excluding the two large negative outliers in Figure 3b. We find no correlation between these variables, including the absence of the U-shape that would be expected if higher turbidity led to an increase in the absolute value of the error.

Finally, ground truthing remotely sensed temperature data for lakes and oceans must contend with the skin-to-bulk temperature effect, in addition to the larger scale thermal stratification that is often present in poorly mixed water. That is, Landsat and other remote sensing temperature detectors measure the temperature of the top ~10 cm of the water, which is influenced by evaporative cooling compared to the bulk temperature beneath the surface (Schluessel et al., 1990; Minnett et al., 2011; Wilson et al., 2013; Javaheri et al., 2016). Because of this evaporative cooling effect, the skin temperature is typically lower than the bulk temperature by <0.5°C (Schluessel et al., 1990). This effect is likely present in our data for Arctic thaw and oxbow lakes. However, disturbances to the surface such as waves are known to decrease the skin temperature effect (Donlon et al., 2002), so while there is an absence of studies on these skin temperature effect for rivers, because rivers are fully turbulent, it likely has a negligible effect on inferring bulk river temperature from the surface (Torgersen et al., 2001).

In summary, we are confident in the ability to use this dataset to identify spatially coherent patterns in the bulk river temperature without correction. The small temperature misfits between our data and in situ gauges are substantially smaller than the spatial and temporal patterns in temperature we analyze. Data shown for lakes, on the other hand, may reflect only surface temperatures modified by skin temperature effects.

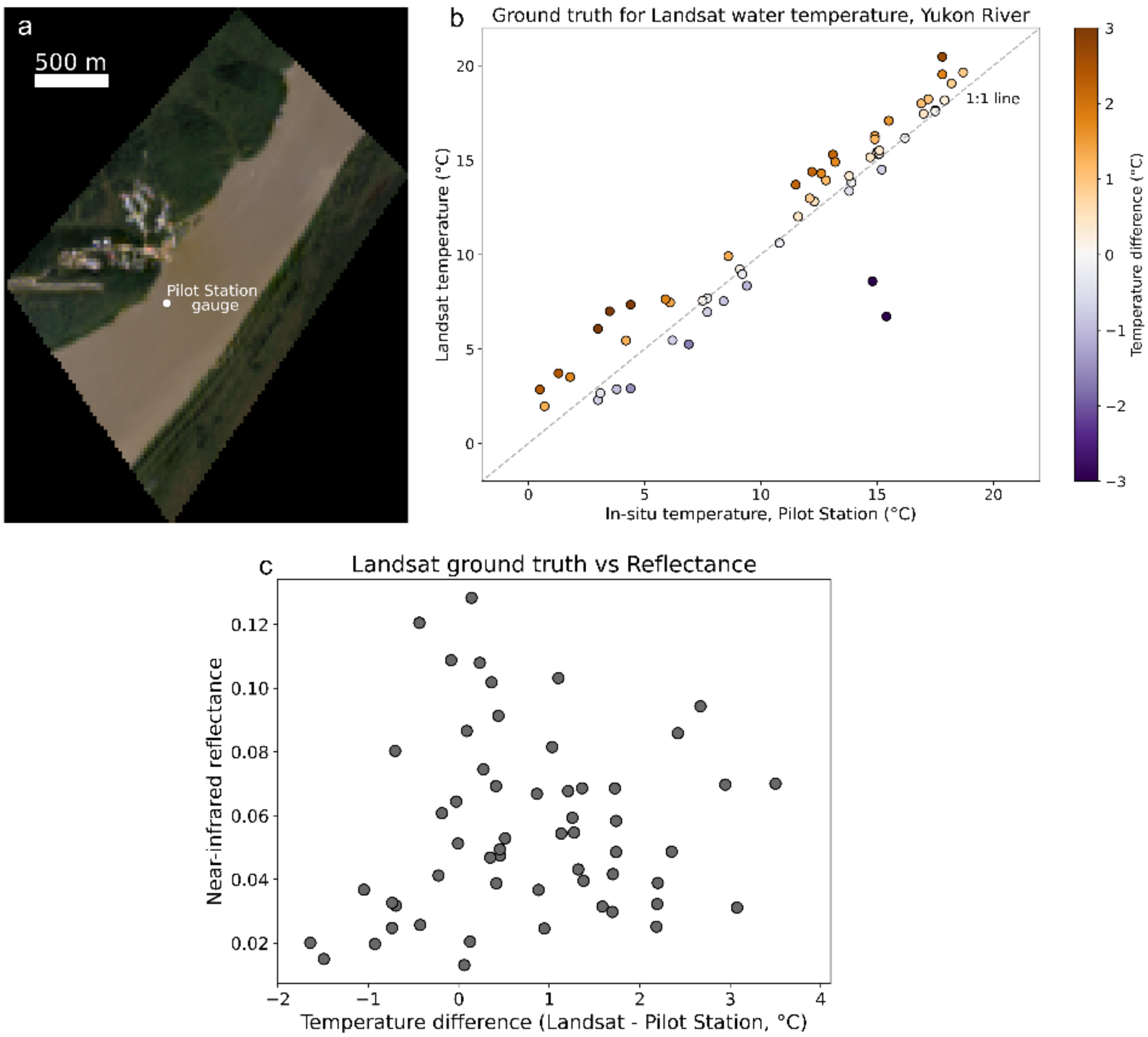

Figure 3: a) The location of the USGS temperature gauge at Pilot Station, station number 15565447, on the Yukon River. The basemap is an RGB image from Landsat 9, and the borders of the image show the region of interest around the gauge delineated for this ground truthing. b) Comparison of temperatures measured in situ by the gauge at Pilot Station to temperatures extracted from the LST calculated from Landsat thermal emission measurements. Each point represents the mean water temperature from one LST image surrounding the gauge location and the contemporaneous gauge temperature and is colored by the difference in value of LST temperature versus in situ temperature. The 1:1 line is plotted for reference. c) The temperature difference between the LST temperature and the in situ temperature vs. the near-infrared reflectance, a proxy for turbidity. Here we have excluded the two large negative outliers <-5°C shown in Figure 3b. No correlation is seen between the LST error and turbidity.

3.2 The Koyukuk River

Using the LST dataset and our water-masking and processing workflow, we generated temperature maps of the meandering stretch of the Koyukuk River near Huslia. We examined spatial patterns in these temperature maps as well as placing these patterns in context of in situ data. The Koyukuk is a major tributary of the Yukon River and allows us to examine patterns in the surface temperature of a meandering, migrating river with several oxbow lakes, including those that are both fully and partially connected to the river, and numerous thermokarst lakes. Figures 4a and b show the Huslia air temperature and Yukon River discharge at the three times we examined compared to typical seasonal values. The air temperature values of the selected dates fluctuate within typical values (Figure 4a). The discharge on the Yukon River at these times are higher than the mean, including outside of one standard deviation for the summer date of 8/30/2016 (Figure 4b).

The water temperature maps demonstrate the surface water temperature varying seasonally and spatially across this meandering riverine corridor. Over the course of an unfrozen season (though as represented by three different years), the Koyukuk's temperature changes from 0–15°C (Figure 4c–e). In the spring, the river is approximately 3°C colder than the air temperature; in the summer, they are almost identical (14°C); and in the fall, the river is 4°C warmer than the air (Figure 4a, c–e). This stretch of the Koyukuk River is surrounded by dozens of small thermokarst lakes that range in size from >900 m^2—the minimum resolvable by Landsat imagery—to approximately 8.5 km^2 (Figure 4c–h). As our data demonstrate, over the course of a season the relative temperatures between the Koyukuk River and these thermokarst lakes change. In the spring and summer, the river is colder than the surfaces of most of the lakes; the difference in temperature is around 5°C in the spring and 2°C in the summer (Figure 4f, g). In the fall, that trend reverses, with the Koyukuk River being 3°C warmer than the surrounding thermokarst lakes (Figure 4h). Figures 4c–h demonstrate that the main channel of the Koyukuk is thermally homogenous at the resolution of the available data. This reflects the thorough mixing of the river as expected for a turbulent water body.

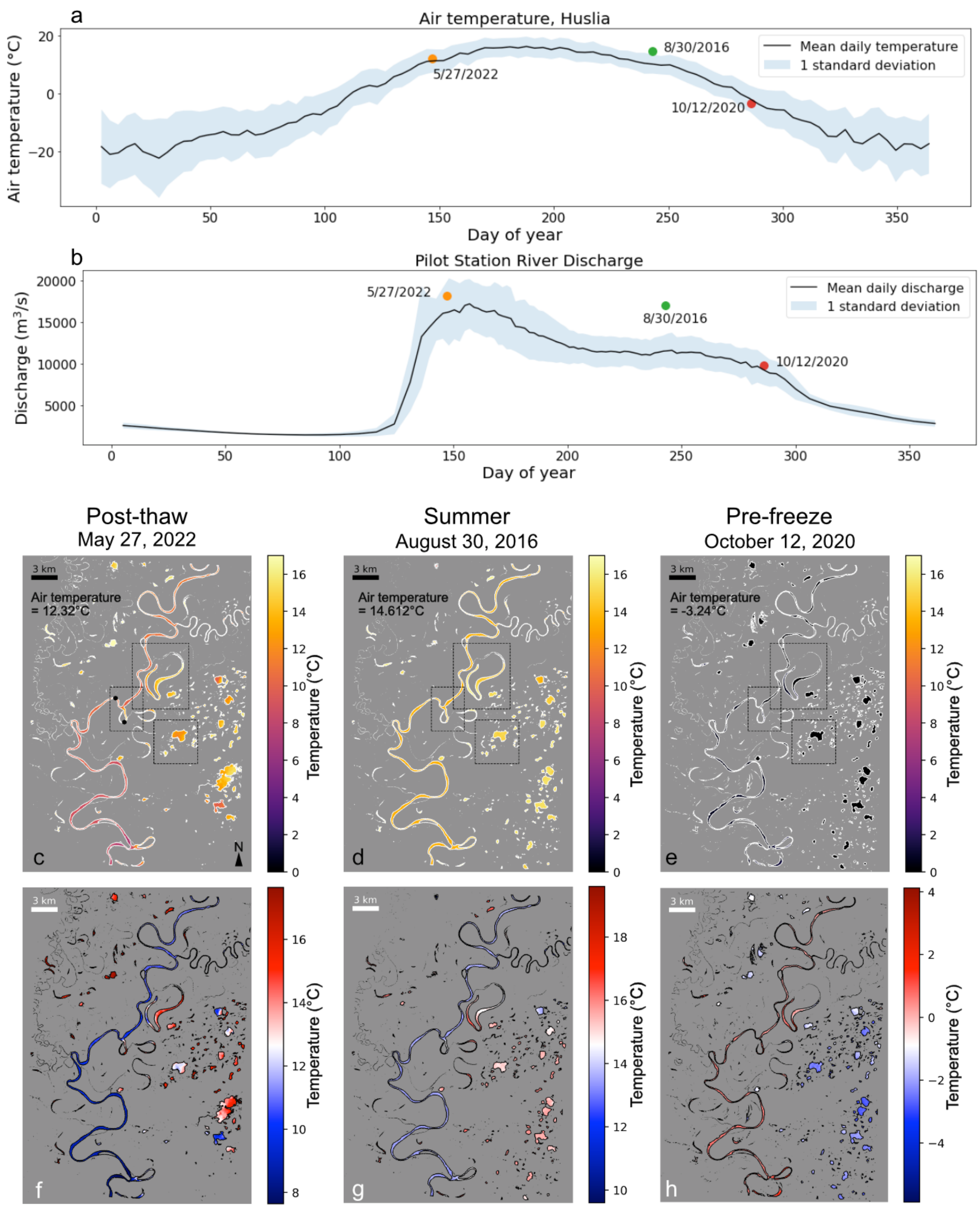

Figure 4: In situ and Landsat data for Huslia on the Koyukuk River. a) In situ mean daily air temperature from 1994–2024 measured by the near-surface temperature sensor at Huslia Airport. b) Mean daily river discharge from 1991–2024 measured by USGS's Pilot Station of the Yukon River. c–e) Processed Landsat water temperature maps of this region across the unfrozen season. The color scale is consistent across these images from 0–17°C, demonstrating relative seasonal changes. The boxes indicate locations of

detailed observations in Figure 5. The black dots in c mark the locations of the in situ HOBO loggers discussed in section 3.1.2. Labeled air temperature measurements correspond to the points in Figure 4a. f-h) Water temperature maps of this region across the unfrozen season with white on the colorbar set at the mean water temperature in the scene. For each, the color scale is ±5°C from the mean. These maps are centered at 65.76°N, -156.36°E. Flow is from north to south.

Our analysis also shows significant temperature variations between the main river channel, oxbow lakes, and adjacent thermokarst lakes that appear to demonstrate their diverse hydrologic processes and water sources. At a given time, the surface temperature of thermokarst lakes across this small area can vary by several degrees (Figure 4f–h). It is particularly evident in the spring, where the temperature of the larger lake, shown in Figure 5a, is approximately 3°C colder on average than the adjacent smaller lakes. Additionally, Figure 5a demonstrates substantial springtime thermal heterogeneity within the larger lake. The surface temperature of the lake at this time ranges from 11.3–14.7°C, a span of 3.4°C. These patterns are not repeated in the summer or fall. Later in the unfrozen season, there are still temperature variations within and between some lakes (Figure 4g, h), but the heterogeneity is smaller within the lakes shown in Figure 5a-c. In the summer and fall, the temperature variation both within and between lakes is on the order of <1°C and may reflect small variations in surface temperature but is likely indistinguishable from the noise of the dataset (Figure 5b, c).

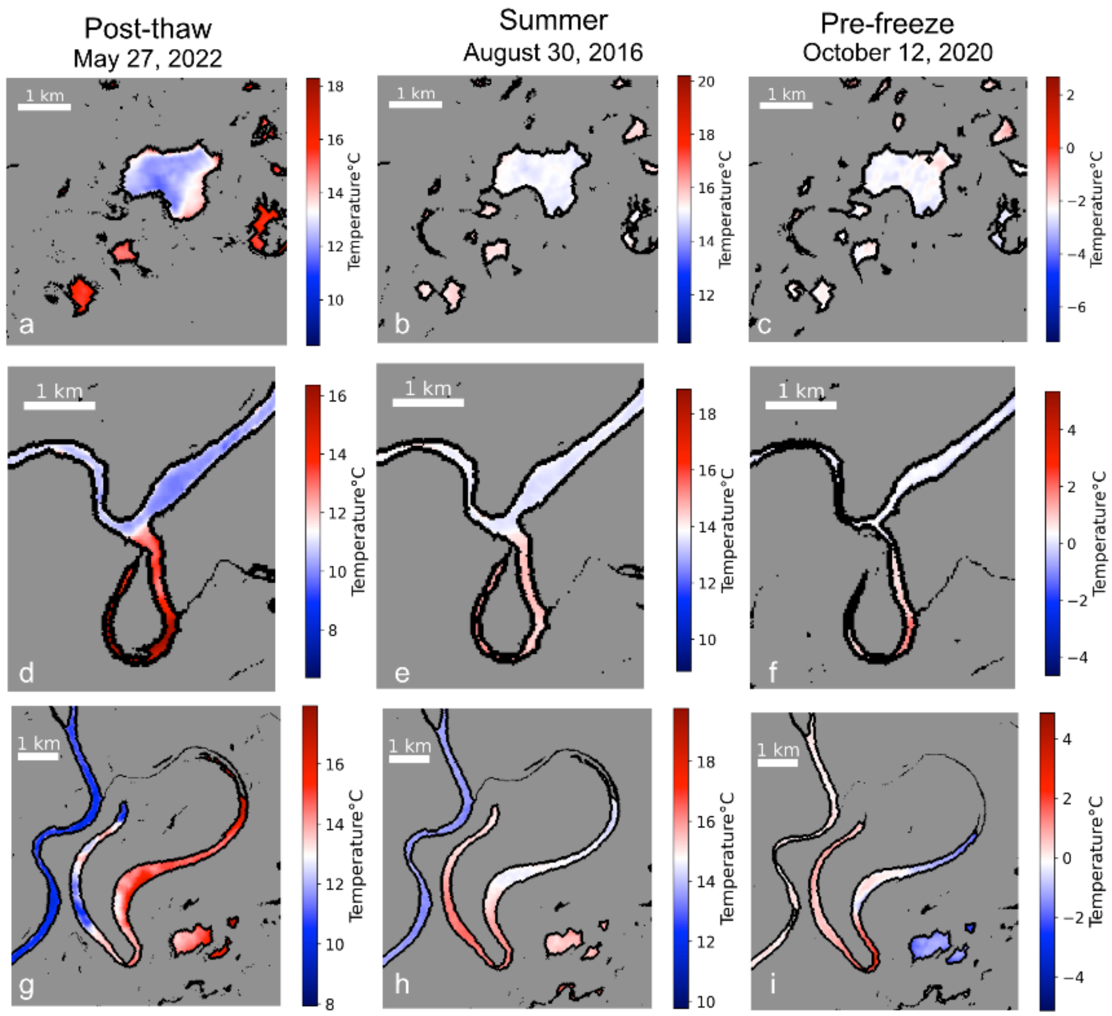

Figure 5: Landsat water temperature maps of locations of interest from the Huslia study site. Temperature colorbars on all maps are set with white at the mean water temperature in the visible extent. a–c) Thermokarst lakes adjacent to the river. d–f) Connected oxbow lake on the main channel of the Koyukuk River. g–i) Sinuous, partially connected oxbow lake on the main channel of the Koyukuk River with significant intra-lake temperature variations.

The temperature maps of the oxbow lake connected to the meandering main channel demonstrate large temperature differences between the lake and the river channel (Figure 5d–f). In all seasons, the Koyukuk River is colder than the surface of the oxbow lake. This generates a temperature gradient across the lake from coldest where the water mixes with the river at the channel connection to warmest most distally. Because this oxbow lake forms a closed loop that is connected to the river channel at one point on both sides, this creates a divergent temperature pattern (the discharge in the fall is low enough that the western side of the lake appears disconnected, but examination of the mNDWI map shows that the western connection remains below the level of detection of the water mask). The magnitude of that gradient varies across season from 5°C in the spring (Figure 5d) to 2°C in the summer (Figure 5e), to 1°C in the fall (Figure 5f).

A close examination of a long, sinuous oxbow lake partially connected to the Koyukuk River reveals an anomalous temperature pattern (Figure 5f–i). It is similar to the temperature pattern seen in the fully connected oxbow lake in Figure 5d–f, but in this case the sinuous oxbow lake is primarily connected to the main channel on the upstream side. Though it was not detected by the water mask, examination of color variation in the visible RGB images indicates that there is a thin <30 m wide stream connecting the downstream side of this oxbow lake to the Koyukuk River in the spring and summer, across which there may be some but likely minimal mixing. In the fall, the lake appears fully disconnected on the downstream side.

In all seasons, our data show that there are substantial (>3°C) temperature variations across the surface of this ~20 km-long oxbow lake. The temperature pattern appears similar in the summer and fall, with the warmest temperatures found near the bend most distant from the river channel and colder temperatures on either side (Figure 5h, i). In the spring, the oxbow lake has the warmest temperatures on the upstream leg of the lake and varying patches of colder and warmer water on the downstream leg (Figure 5g). The visible image of this lake reveals that the summer temperature patterns closely follow the color of the surface water, with the lighter/brown colors indicating more turbid water and the darker/green colors indicating less turbid water, as shown in Figure 6. Turbidity should not substantially affect Landsat's measurement of the surface temperature, as discussed in Section 3.1, so the corresponding patterns of these parameters suggest that both temperature and turbidity are demonstrating the hydraulics of the lake and river mixing.

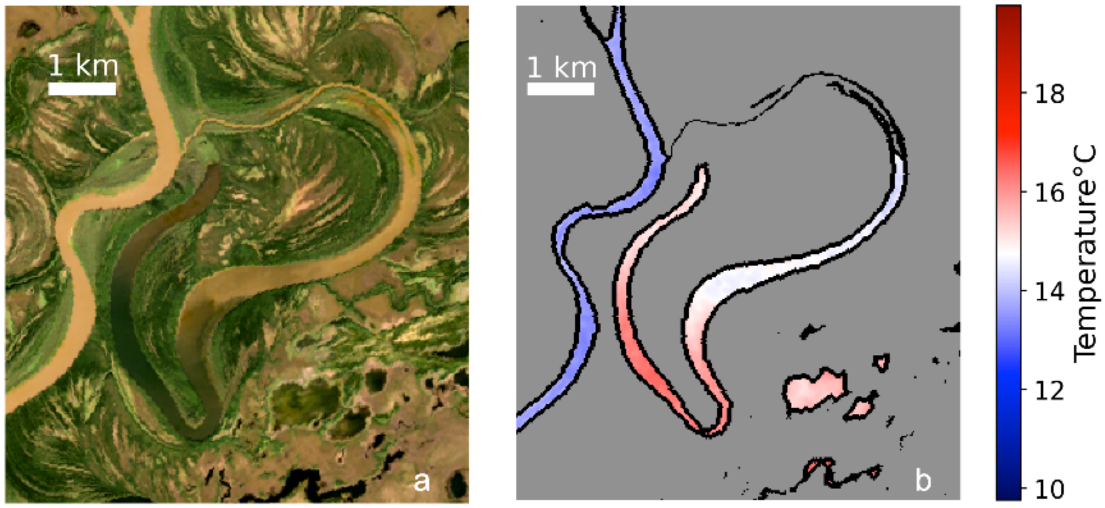

Figure 6: a) Enhanced visible RGB image of the sinuous oxbow lake on the Koyukuk River taken on August 30, 2016. b) Detailed view of Figure 5h, showing the same date as 6a. The color scale is set with white at the mean water temperature in the visible extent.

3.2.1 Comparing surface temperature to temperature at depth

We also compared the surface water temperature as measured with the LST dataset to the in situ water temperature several meters below the surface. Over the 2023 unfrozen season, in situ water temperature data were collected continuously using HOBO temperature loggers at several sites on the Koyukuk River near Huslia. These loggers were anchored a few centimeters above the riverbed, so the depth varied with the river stage. The in situ temperature was consistently measured every 15 minutes, from which we calculated the daily mean temperature for each logger. We compared the surface and deep temperatures for two locations indicated in Figure 4c: an oxbow lake (Figure 5d–f) and within the main Koyukuk channel 5 km downstream of the oxbow lake (Figure 4c). We compared these values to the mean instantaneous surface temperature of a small cloud-free area extracted from Landsat images taken on the same day around the location of the logger. We were limited to <10 data points from each location due to cloud cover. For each, we plotted a linear regression of the difference in temperature between the surface and at depth versus the date and versus the water depth recorded by the logger (Figure 7).

For the main channel, the temperature differences between the surface and depth (13–18 m) are small. In many cases, the surface and deep temperatures are essentially equal (within the uncertainty of the absolute accuracy of the remotely sensed and in situ temperature measurements) (Figure 7a–c). The remotely sensed surface values tend to be slightly higher than the deep temperatures where there are small differences, which may be in part due to the small positive bias in the remote sensing measurements. There is a substantial difference between the surface and deep temperature on August 10, and it is unclear why, but must be related to a transient and local cold water plume. Excluding the one outlier, there appears to be no systematic correlation between surface versus deep temperature difference with day during the summer (Figure 7b) nor with depth of the river (Figure 7c). This is indicated by the low slopes of their respective linear regression fits (fit without the outlier). We interpret that this indicates the expected turbulent mixing of the river.

For the oxbow lake, the surface temperatures are consistently higher than the temperatures measured at depth (10.15–15.43 m). Temperature differences between the surface and at depth range from 0.37 to 6.38 °C (Figure 7d). There does not appear to be a correlation between the temperature difference and the date, as indicated by the low regression slope and r^2 value. There is positive correlation between the temperature difference and the depth of the logger, with smaller temperature differences for days where the logger depth was smaller. The slope fit to this relationship for the oxbow lake is an order of magnitude greater than that for the channel (Figure 7c, f). We interpret these observations as demonstrating the thermal stratification of this oxbow lake. This stratification was somewhat more pronounced when the lake was deeper, showing a larger thermal gradient (Figure 7f). There appears to be little correlation between date and thermal stratification (Figure 7e). These data were taken from June to August, which likely represents a similar thermal regime, as data collection begins after complete ice melting and ends well before the initiation of re-freezing.

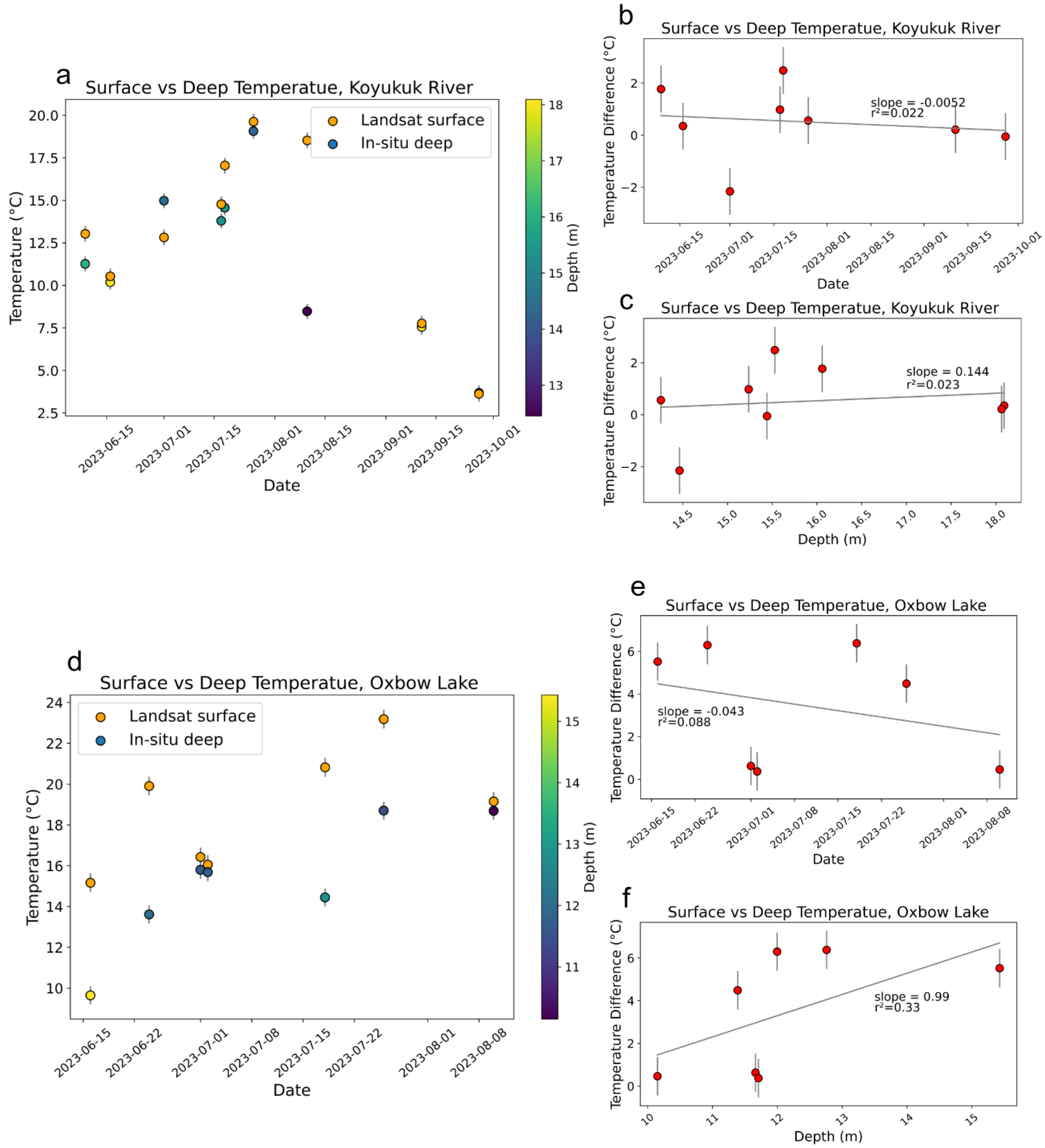

Figure 7: A comparison of surface water temperature extracted from the LST to in situ measurements taken at depth by HOBO loggers. The error bars on the Landsat measurements are ±0.46°C, the mean error of the LST dataset compared to the Pilot Station in situ temperatures. a–c) Surface temperature vs. temperature at depth on the main channel of the Koyukuk River. Trendlines plotted in (b) and (c) were calculated without the large outlier temperature value recorded in August by the in situ logger. d–f) Surface temperature vs. temperature at depth for the distal portion of the oxbow lake examined in detail in Figure 5d–f.

3.3 The Yukon-Tanana River confluence at Tanana town

We next examine patterns of surface water temperature at the confluence of the Yukon and Tanana Rivers. At the point of confluence, both rivers are anastomosing. The Yukon flowing dominantly northeast–southwest, and the Tanana flows southeast–northwest before both join into the westward-flowing Yukon River. We focus on examining the contemporaneous relative temperatures of these two rivers as well as the thermal structure of the Yukon downstream of the confluence. Remote sensing provides the unique opportunity to gain a comprehensive view of the spatial distribution of temperature and length of mixing in such a confluence. Figures 8a and b indicate the air temperature at this confluence (Tanana town) and the downstream Yukon River discharge at the three dates we examined compared to typical seasonal values. The air temperature on the post-thaw date of 5/19/2021 is slightly higher than one standard deviation from the mean of this date, but all other temperature and discharge values are within the one standard deviation envelope.

We first compare the temperature of the river water to that of the air. The three dates examined here show that Yukon and Tanana River temperatures vary from approximately 3–14°C over the unfrozen season (Figure 8c–e). Like the Koyukuk River (Figure 4), these rivers are colder than the air temperature in the spring by up to 7°C, nearly identical in the summer (~15°C), and warmer than the air temperature in the fall by 5°C (Figure 8a, c–e).

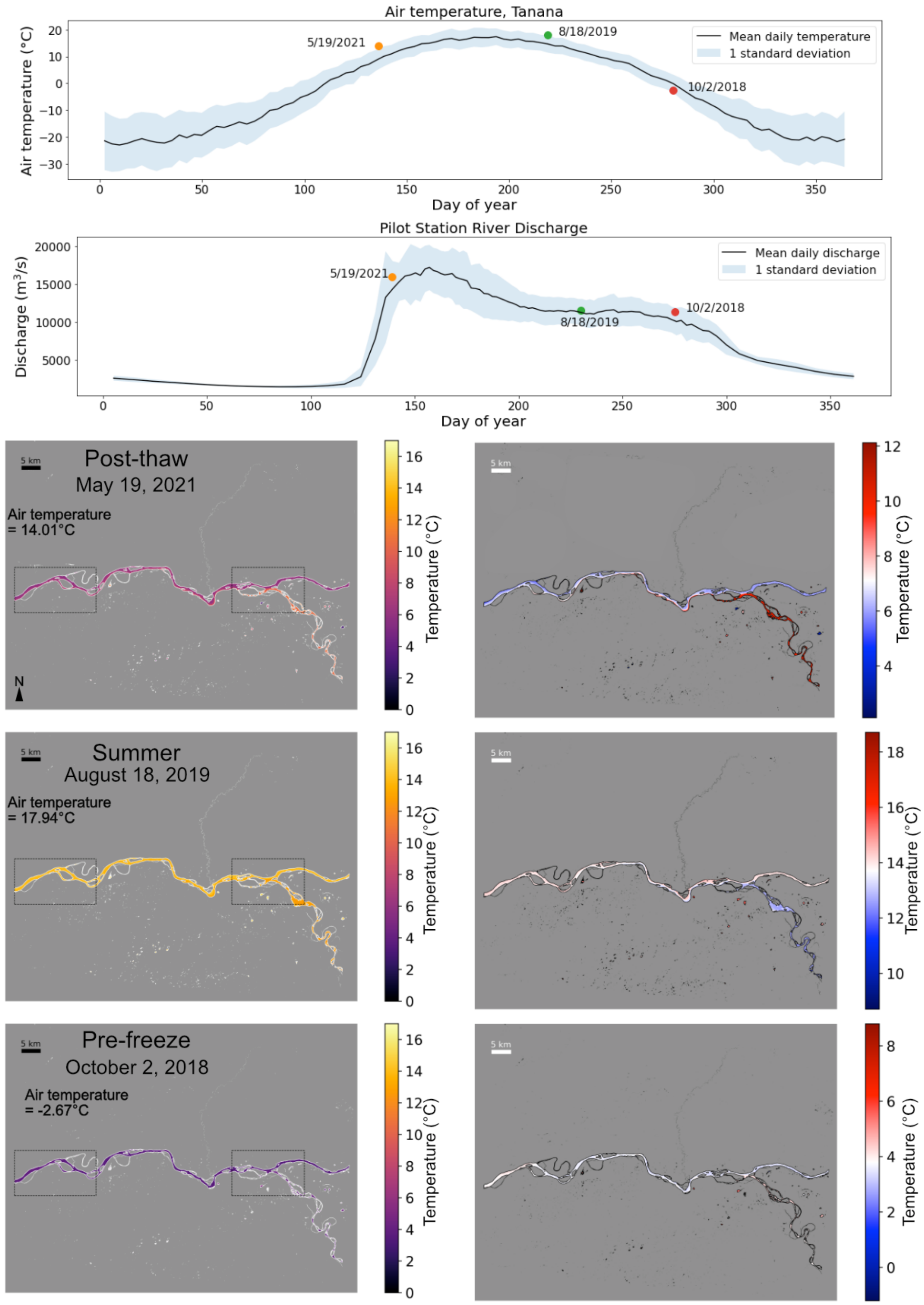

Figure 8: Data for Tanana town at the confluence of the Yukon and Tanana rivers. a) Mean daily air temperature from 1943–2024 present measured by the near-surface

temperature sensor at Ralph M Calhoun Memorial Airport. b) Mean daily river discharge from 1991–2024 measured by USGS's Pilot Station of the Yukon River. c–e) Landsat water temperature maps of this region across the unfrozen season. The color scale is consistent across these images from 0–17°C, demonstrating relative seasonal changes. The boxes indicate locations of detailed observations in Figure 9. Labeled air temperature measurements correspond to the points in Figure 8a. f–h) Water temperature maps of this region across the unfrozen season with white on the colorbar set at the mean water temperature in the scene. For each, the color scale is ±5°C from the mean. These maps are centered at 65.18°N, -152.63°E. Flow is from right to left.

We focus on comparing the relative temperatures of the two rivers at the point of intersection (Figure 9a–c) and 100 km downstream from the confluence (Figure 9d–f). As expected, each river individually is largely thermally homogenous before the intersection. Because of the introduction of a new source of water at the confluence, the combined Yukon then becomes thermally heterogenous (Figure 9a–c). Throughout the unfrozen season, the relative temperatures of these two rivers changes. In the spring and fall, the Yukon is colder than the Tanana, by margins of ~5°C and ~1°C, respectively (Figure 9a, c). In the summer, the Yukon is ~1.5°C warmer than the Tanana (Figure 9b).

Downstream of the confluence where both rivers merge into the Yukon River, the cross-sectional temperature variation decreases until the two rivers are fully mixed. In the summer and autumn, the rivers have thermally homogenized at a distance of 100 km from the confluence (Figure 9e, f). This is indicated by the lack of detectable lateral thermal gradient across the Yukon on these dates. In the spring, where there is the greatest initial difference in the river temperatures, there is still an apparent temperature gradient of ~2°C across the river 100 km from the confluence (Figure 9d).

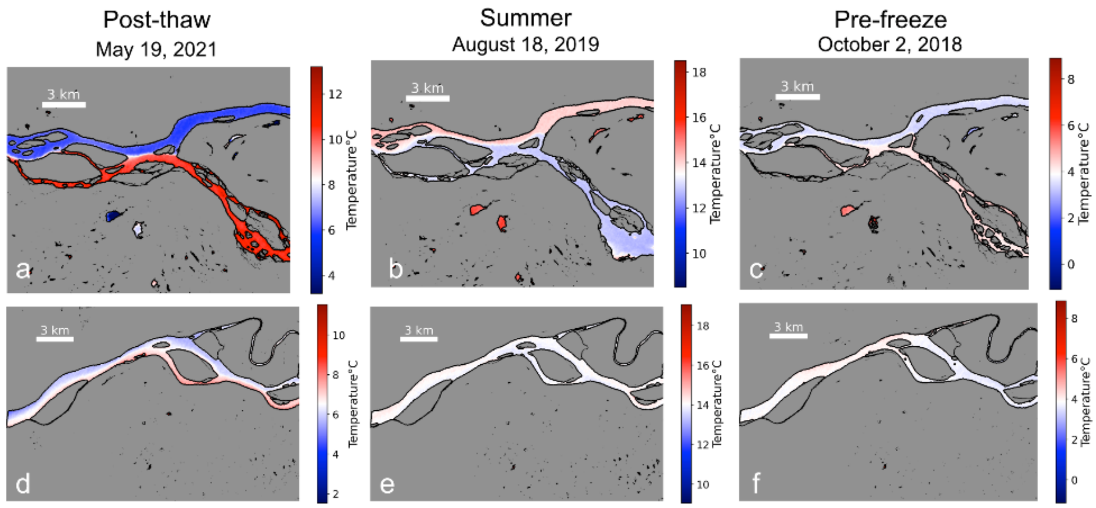

Figure 9: Water temperature maps of locations of interest from the Tanana town study site. Temperature colorbars on all maps are set with white at the mean water temperature in the visible extent. a–c) Initial contact of the confluence between the Yukon River (northern branch) and Tanana River (southern branch). d–f) Stretch of the Yukon River 100 km downstream of the confluence. Flow is from right to left.

We interpret these temperature maps as demonstrating the forces affecting water temperature of these two rivers. The temperature patterns suggest that for rivers in the Arctic, where there are especially large seasonal and latitudinal temperature variations, relative contemporaneous temperatures of the water bodies are set primarily by latitude and secondarily by water source. The Yukon River traverses higher latitudes before the confluence, while the Tanana River flows from lower latitudes. Warmer air temperature arrives earlier to the lower latitudes in the spring, which would increase the temperature of the Tanana River at these lower latitudes relative to the higher-latitude, colder water of the Yukon River. Similarly, warmer air temperatures persist longer into the autumn at the lower latitudes, leading to warmer water temperature in the Tanana River in the autumn. We propose that this process is reflected in the relatively colder temperatures of the Yukon in the spring and autumn (Figure 9a, c). In the summer, air temperature is more consistent across these two watersheds. At this time, the Yukon River is 2°C warmer than the Tanana (Figure 9b). We hypothesize that this is due to the varying contributions of different water sources including snow meltwater, rainwater, and groundwater. At the confluence, the Yukon has flowed thousands of km from its source of high-elevation glacial lakes, and most of its traverse was across low-elevation terrain. This yields warmer water temperatures. The Tanana is more immediately sourced from meltwater in the Alaska Range mountains, which is consistent with its colder water temperature in the summer. More rigorous modeling would be needed to determine the exact contributions of various water sources and thermal forces on a given river.

Additionally, this site demonstrates how remotely sensed temperature maps can illustrate how temperature acts as a proxy for the mixing of water bodies due to both physical mixing and thermal diffusion. At the point of confluence, the physical separation between the rivers is sharp, as shown by the distinct difference in temperature across the river cross-section (Figure 9a–c). Downstream, the cross-sectional temperature variation decreases until the two rivers are fully mixed. This turbulent mixing length scale is primarily a function of the relative discharges of the two rivers and their miscibility due to differences in density caused by suspended sediment content and temperature (e.g. Kenworthy and Rhoads, 1995; Konsoer and Rhoads, 2014; Pouchoulin et al., 2020). In the summer and autumn, the rivers have fully thermally mixed at a distance of 100 km from the confluence (Figure 9e, f). In the spring, likely due to the greater initial difference in the river temperatures, there is still an apparent temperature gradient across the river 100 km from the confluence (Figure 9d). Remote sensing of turbidity has been used to examine mixing at river confluences (e.g Umar et al., 2018), and our results support that temperature can also be used to track these hydrodynamic processes.

3.4 The Yukon River at Beaver

Lastly, we generate and examine water temperature maps of a stretch of the Yukon River near Beaver. This region represents the typical anastomosing morphology of the Yukon. Figures 10a and b indicate the local air temperature and the downstream Yukon River discharge at the three times we examined compared to typical seasonal values. All temperature and discharge values on the dates examined are within one standard deviation of their mean values except for the discharge on the pre-freeze date of 10/7/2019, which is slightly lower than typical values.

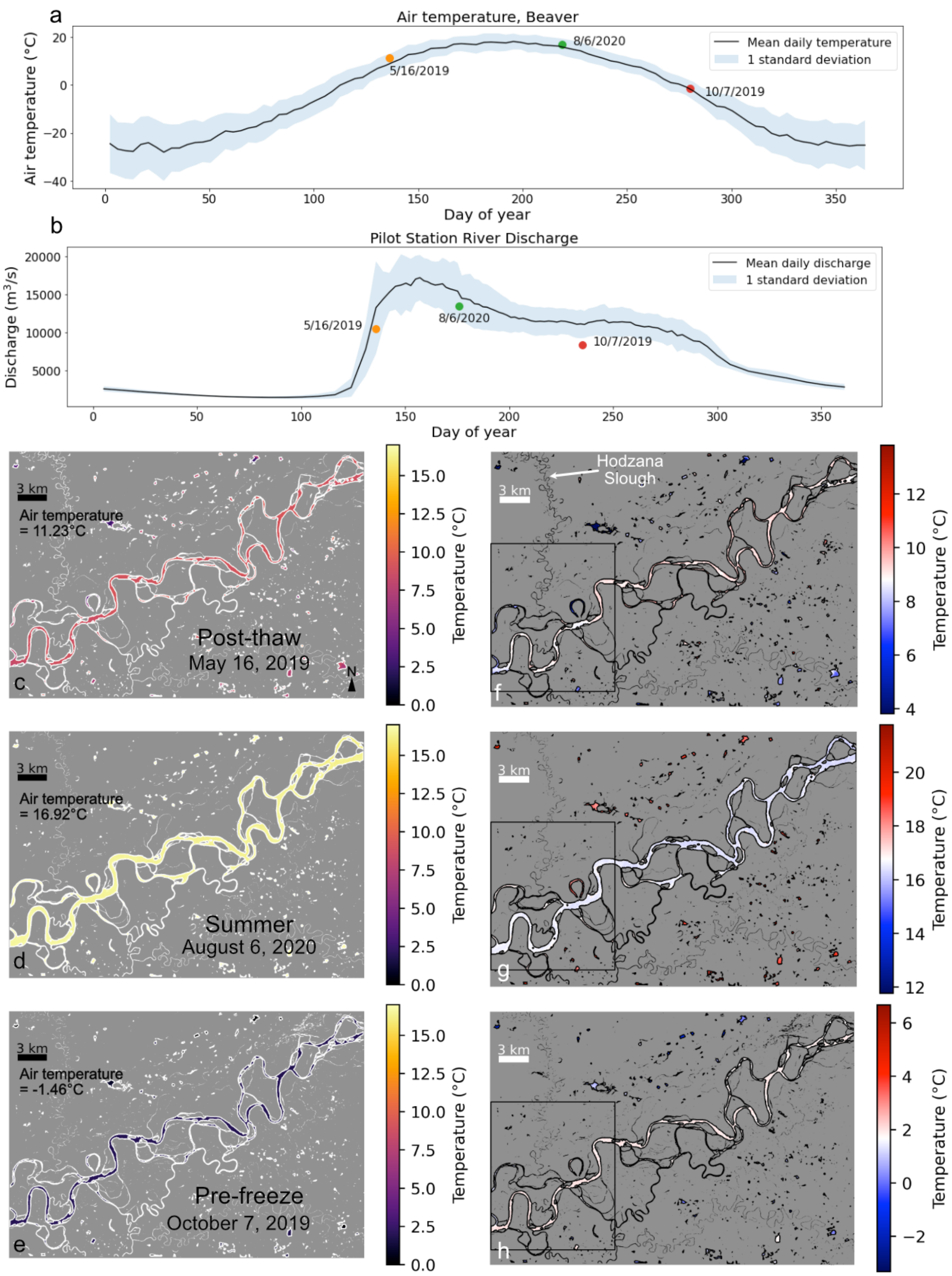

Figure 10: Data for Beaver on the Yukon River. a) Mean daily air temperature from 1948–2024 present measured by the near-surface temperature sensor at Fort Yukon Airport. b) Mean daily river discharge from 1991–2024 measured by USGS's Pilot Station of the Yukon River. c–e) Water temperature maps of this region across the unfrozen season. The color scale is consistent across these images from 0–17°C, demonstrating relative seasonal changes. The boxes indicate the location of the detailed

observation in Figure 11. Labeled air temperature measurements correspond to the points in Figure 10a. f–h) Water temperature maps of this region across the unfrozen season with white on the colorbar set at the mean water temperature in the scene. For each, the color scale is ±5°C from the mean. These maps are centered on 66.345°N, -147.40°E. Flow is from northeast to southwest.

Consistent with the other locations examined, this stretch of the Yukon River is largely thermally homogenous at this resolution. Near Beaver, the Yukon River is anastomosing with a complex geometry composed of numerous river threads and sloughs. Despite these numerous channels, our generated water temperature maps demonstrate that the surface water temperature of the major anastomosing reaches is approximately constant across the whole stretch indicating a high degree of connectivity (Figure 10d–h). Where and when sloughs and secondary channels are wide enough for their temperature to be measured accurately, such as late spring–summer, temperatures also closely match that of wider threads. One deviation from this homogeneity is a slight decrease in temperature on the downstream end of the river in the spring and fall (Figure 11a, c). Temperature decreases after the intersection of the Yukon with the small Hodzana Slough flowing into it from the north. In the summer, there is no detectable decrease in temperature after the confluence (Figure 11b).

Similar to our observations of oxbow lakes in Huslia, the oxbow lake along the Yukon shown in Figure 11 typically differs in temperature from the adjacent river. In the spring, the lake is ~3°C colder than the river; in the summer, the lake is ~2°C warmer than the river; and the temperatures of the two are comparable in the fall. Unlike in Huslia, this oxbow lake is largely or entirely disconnected from the river. Therefore, we do not observe, nor do we expect to observe, a robust relationship between surface water temperature and distance from the river as we did in Huslia (Figure 5d–f). Rather, the oxbow lake near Beaver appears to behave analogously to other floodplain lakes in the region. We interpret the surface temperature of these lakes to reflect vertical thermal stratification and internal mixing processes as in the other study locations.

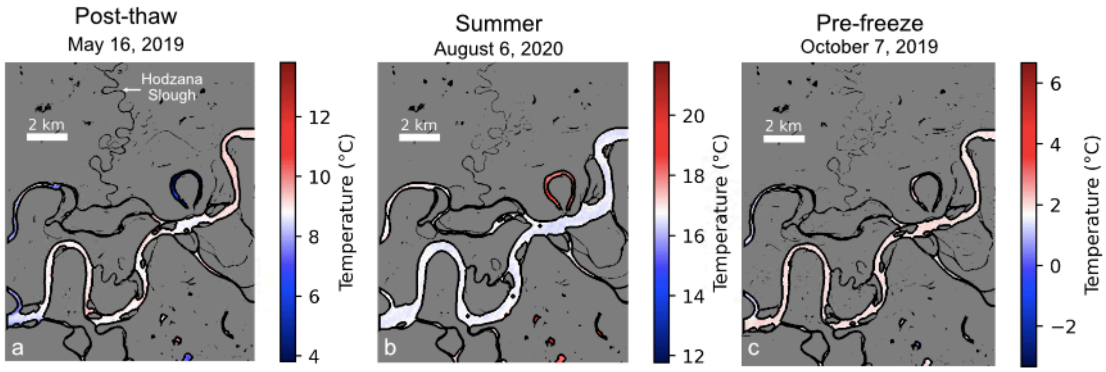

Figure 11: Water temperature maps of a location of interest from the Beaver study site. Temperature colorbars on all maps are set with white at the mean water temperature in the visible extent. a–c) Downstream portion of this short anastomosing stretch of the Yukon River, before and after the intersection with the Hodzana Slough.

4 Discussion

4.1 Vertical temperature structure

By comparing the remotely sensed surface water temperature measured by the LST to in situ temperature measured at depth, we can contrast the vertical temperature structure of Arctic rivers and lakes and identify how remote sensing can be appropriately applied to understand water temperature of river corridors. The expectation is that rivers should be thermally well-mixed vertically because they are fully turbulent (Franca and Brocchini, 2015). This is supported by our comparisons of LST to both the in situ Pilot Station gauge on the Yukon River and the HOBO logger anchored at depth in the Koyukuk River. The similarity of the temperature measured at the surface by LST and at depth by an in situ gauge (Figure 7a) demonstrates that there is no clear thermal stratification of the river channel, and it is well-mixed throughout the vertical profile. This also indicates that rivers either lack an evaporative cooling thermal skin effect as has been theorized (Torgersen et al., 2001), or that if it exists, it is within the LST uncertainty. This result demonstrates the power of remote sensing for applications to measuring and understanding river water temperature. By measuring the temperature of just the top 10 cm of the water, the LST can accurately capture the temperature of the entire river water column.

Conversely, our results demonstrate that while remote sensing surface temperature can yield valuable information about lake surface temperature, it does not reflect the thermal behavior at depth. This is demonstrated by the difference in the oxbow lake surface water temperature measured by LST and the temperature at depth measured in situ, with higher temperatures at the surface indicative of thermal stratification (Figure 7d). This is expected for lakes of this depth, as lakes >10 m deep typically exhibit steep thermoclines (Gorham and Boyce, 1989; Boehrer and Schultze, 2008; Pöschke et al., 2015; Cannon et al., 2019). Therefore, while remote sensing can be used to accurately measure the water temperature at a lake's surface, for water bodies that can achieve stratification, in situ observations are required to understand the temperature at depth.

4.2 Seasonal patterns in water temperature

Because LST provides high-resolution temporal coverage (repeat observation time is typically 1–7 days), our data demonstrate how surface water temperature within these Arctic riverine corridors evolves seasonally. We find that the dates we examined from post-ice breakup to pre-freezing capture the large swings in water temperature these rivers experience over the course of the unfrozen season. All rivers demonstrate >10°C swings in water temperature over the season, from just above freezing to an average temperature of ~15°C. By comparing the remotely sensed LST temperature values with those of in situ air temperature monitors, we see that this water temperature evolution is similar to the magnitude of the air temperature variation.

Despite the differences in hydrological context of these rivers including elevation, permafrost distribution, and geometry both locally and in their upstream watersheds, the three sites examined here appear to largely track local air temperature well. In all locations, there is a clear offset in water temperature compared to air temperature in the spring and fall of 3–7°C due to water's higher thermal inertia but a close match of water and air temperature (0–4°C) in the summer (Figure 4, 8, 10).

However, within the examples we examine here, we do observe significant deviations from this close correlation of river temperature to air temperature. At the confluence of the Yukon and Tanana Rivers, there is a ~5°C difference in water temperature between rivers despite the same local air temperature (Figure 9a). While the temperature of both rivers evolves over the course of the season correlated with air temperature, the water temperature difference between them indicates the additional controls on river temperature besides local air temperature and thermal inertia, which we argue include water source and upstream watershed air temperature.

Lake surface water temperature varies substantially within a river corridor at a given time, and so while all lake temperatures do evolve systematically with air temperature across the unfrozen season, they are more decoupled from the air temperature than rivers are (e.g. Figure 4). The seasonal evolution of lake surfaces appears to be strongly controlled by mixing and stratification processes in addition to larger-scale regional trends in air temperature.

We also compared the water temperature to a relative estimation of the local river discharge, as represented by the discharge measured in situ at Pilot Station on the Yukon River. River discharge also varies seasonally, from its highest values just after ice breakup to a fairly consistent plateau until refreezing (Figure 4b, 8b, 10b). If river water temperature varies with discharge, it is more subtle compared to the strong correlation to air temperature. More data including local discharge measurements would be required to disentangle the effects of discharge on river temperature.

4.3 Spatial patterns in water temperature

By providing complete spatial coverage, it is clear that LST can be used to examine the spatial patterns in surface water temperature across riverine corridors. Our primary observation of river temperature is that—excluding the introduction of a new source of water to the river—water temperature is largely homogenous across the 50–100 km long stretches examined. The surface temperatures of these stretches of the Koyukuk, Yukon, and Tanana rivers appears to vary by <1°C, within the uncertainty of the LST measurements. This consistency in surface temperature is evident across river contexts and morphology including meandering (Koyukuk River) and anastomosing (Yukon River) stretches. Even in locations with complex geometry such as the anastomosing region near

Beaver, there is thermal homogeneity across the threads, secondary channels, and sloughs that are large enough to be measured with this method (Figure 9f–h).

However, the spatial coverage provided by remotely sensed imagery captures well where there are deviations from this homogeneity in both connected and disconnected water bodies. In particular, we observe that the introduction of a new source of water can create thermal heterogeneities. This is particularly evident at the confluence of the Yukon and Tanana rivers, where the mixing of these different water sources creates a lateral temperature gradient across the combined Yukon River that can still be detectable even up to 100 km from the point of confluence. The remotely sensed temperatures we generated for this study demonstrate how temperature acts as a proxy for the mixing of water bodies due to both physical mixing of the water masses and thermal diffusion. Remote sensing of turbidity has been used to examine mixing at river confluences (e.g Umar et al., 2018), but these results indicate that temperature alone can also be used to track these hydrodynamic processes. This can be used alongside turbidity to separate the effects of physical mixing and thermal diffusion, and it may be useful to understand tributary mixing even if there is no substantial turbidity difference between the rivers.

Lakes in these Arctic river corridors demonstrate different patterns in spatial distribution of surface water temperature depending on their depth and their connectivity to rivers. In particular, we observe that the surface temperature spatial patterns of connected oxbow lakes are distinct from that of disconnected thermokarst lakes. This is likely a function of both their hydrologic connectivity and size. Arctic lakes exhibit variable mixing processes depending on their size and structure. Deep lakes are typically dimictic, experiencing wind-driven overturn twice a year but stagnation and stratification in the summer (Gorham and Boyce, 1989; Boehrer and Schultze, 2008; Pöschke et al., 2015; Cannon et al., 2019). Lakes that are sufficiently shallow (< ~10 m) tend to be polymictic, that is, wind can mix the full volume more continuously (Taranu et al., 2010; Pöschke et al., 2015). Our surface temperature maps of the oxbow lake examined near Huslia show a temperature gradient across its surface that appears to track the mixing of the lake water with the main river channel (Figure 5d–f). This thermal stratification is also illustrated by the comparison of the remotely sensed surface water temperature to the water temperature measured in situ at depth (Figure 7d).

The surface temperature maps of the thermokarst lakes demonstrate the control of mixing and other local processes on these shallow water bodies. We observe that adjacent lakes of similar surface area in Huslia (Figure 4f–h) as well as near Tanana town (Figure 9a–c) and Beaver (Figure 10) can vary in temperature by nearly 5°C. Therefore, the remotely sensed surface temperatures likely demonstrate the effects of additional processes beyond the control of air temperature. These processes likely include discontinuous permafrost distribution or mixing processes, and more detailed data would be required to constrain all processes impacting the surface temperature of these lakes. Our data demonstrate that for an Arctic floodplain environment, where these thermokarst lakes are abundant, remotely-sensed temperature maps capture thermal diversity in lake temperature that would not be captured effectively by sparse in situ point measurements.

4.4 Applications of remotely sensed water temperature to the Arctic

Thermal remote sensing of water temperature has a wide array of potential applications to Arctic environments. The remotely sensed water temperature maps we created demonstrate the variability of contemporaneous water temperature across riverine corridors, seasonal temperature changes, and mixing of water bodies and hydraulic connectivity.

An important application of these maps is providing an understanding of the temperatures experienced by different organisms in the ecosystems in and around these bodies of water. In particular, remote sensing of river temperature in Alaska provides critical information about thermal stresses on salmon, which have declined sharply in recent years (e.g. Jacob et al., 2010; Westley, 2020; Thorstad et al., 2021; Biela et al., 2022). Many studies that attribute salmon decline to rising river temperature rely solely on air temperature data as a proxy for water temperature, but remote sensing can be used to understand actual water temperatures encountered by salmon on their migration from the ocean upriver to their breeding grounds and catalog potentially life-saving thermal refuges (Bilby, 1984; Ebersole et al., 2003; Torgersen et al., 2012). High-resolution (cm-scale) thermal imaging from airborne platforms has been used to identify smaller thermal refuges on the ~1 m scale (e.g. Torgersen et al., 2012; Frechette et al., 2018), but with our data, we are able to identify larger possible refuges without need for the expense of dedicated surveys. In particular, we identify anomalously cold regions of rivers at confluences with tributaries or even small sloughs. For example, at the Yukon-Tanana confluence, the Tanana River brings in water 2–3°C colder than the Yukon that significantly cools the stretch of the river downstream of the confluence (Figure 8), and even the Hodzana Slough significantly cools the river near its intersection with the Yukon River at Beaver (Figure 11).

In permafrost-rich environments such as the Arctic, the remotely sensed water temperature data with high spatial and temporal resolution can be used to help characterize and predict the rate of riverbank erosion, as a relationship has been found between river water temperature and bank erosion rate (Costard et al., 2003; Douglas et al., 2023; Geyman et al., 2024). Because we show that the surface water temperature measured by satellites is a good representation of the water temperature at depth (Figure 7a), our results demonstrate that LST can be used to measure the temperature of the water that is eroding permafrost-bearing banks. For example, we show that the water temperature of the meandering Koyukuk River lags behind the air temperature in the spring after ice breakup (Figure 4), when river discharge is highest and erosion has been found to be substantial (Geyman et al., 2024). In this case, the rate of bank erosion is likely thermally-limited by the cold water's ability to melt the cohesive permafrost. Later in the summer, the water temperature warms rapidly to match or exceed that of the air, but the discharge is comparatively low. This likely creates transport-limited bank erosion, where the water is able to melt the permafrost but does not have the power to transport away the thawed sediment. This is consistent with remote sensing observations of the timing of bank erosion in this region (Geyman et al., 2024) and demonstrates that remote sensing of water temperature can be used to provide critical constraints on riverbank erosion rates, particularly as permafrost continues to degrade due to climate change.

Additionally, understanding the spatial distribution of surface water temperatures allows for more accurate calculations of geochemical fluxes such as greenhouse gas release from rivers and lakes. Constraining these processes is particularly necessary in the Arctic, where permafrost thaw is driving release of organic carbon (Zandt et al., 2020). Quantifying thermokarst lake temperature is necessary to calculate chemical fluxes such as greenhouse gas release from these water bodies, but we demonstrate that remote sensing cannot be used to measure water temperature at depth. However, we also show that the remotely sensed temperature maps can capture significant (>5°C) variations between the surface temperatures of adjacent lakes (e.g. Figure 5, Figure 9a), likely reflect variations in the timing and process of lake overturn and mixing. Measurement of water temperature throughout the water column and at depth requires the placement of sensors, which is a challenging and expensive process, especially in the remote Arctic. Our maps demonstrate that remote sensing can be used to guide those placements, for example by identifying lakes that appear representative of the typical thermal state of lakes in a region or by identifying unusual, thermally anomalous lakes. By capturing the contemporaneous surface water temperature across a floodplain, remote sensing can also be used to help extrapolate from in situ point measurements across the region. This can support robust calculation of greenhouse gas fluxes from this crucial source that is predicted to pose significant impacts on the climate.

Remote sensing like the LST dataset can be combined with state-of-the-art models to both fill in gaps in the remote sensing and in situ gauge datasets as well as to predict future changes to river temperature. For example, Chang et al. (2025) combine atmospheric and climate data from ERA5-Land reanalysis (Muñoz-Sabater et al., 2021) with the AKTEMP collection of gauge temperature data. This succeeds in predicting river temperature well, and future work could construct similar models relying on the LST data as the input to expand coverage further beyond the available gauges in Alaska, such as has been implemented with LST in other locations (e.g. Al-Murib et al., 2019; Murphy et al., 2021). Additionally, future work should take advantage of LST's four decade-long temporal record, which is longer than most gauge records, in addition to its spatial coverage. This allows analysis of long-term thermal evolution across diverse contexts, including climate change-driven trends (e.g. Santos Fleischmann et al., 2025).

5 Conclusions

Understanding water temperature in Arctic rivers and wetlands is essential for predicting permafrost thaw, river erosion, greenhouse gas emissions, and ecosystem health, yet existing observations from in situ gauges and airborne surveys remain spatially limited and difficult to obtain in this remote region. Here we demonstrate the power of the Landsat Land Surface Temperature (LST) dataset for resolving the spatial and seasonal patterns of surface water temperature across Arctic river corridors and their surrounding wetlands. We find that LST can successfully measure temperatures for water bodies wider than ~210 m, with smaller water bodies affected by mixed land–water thermal signals. For sufficiently large rivers and lakes, comparison with in situ measurements demonstrates that LST is reasonably accurate, with a median error of 0.46°C. Across three distinct Yukon River watershed environments in Alaska, we show that remotely sensed surface temperatures closely represent bulk river temperatures, whereas lakes may experience thermal stratification and skin temperature effects that are not captured by remote sensing alone. Water temperatures largely track seasonal air temperature variations, but with a lag caused by water's thermal inertia, and exhibit substantial (~15°C) seasonal swings characteristic of high-latitude climates. Spatially continuous temperature maps reveal that river temperatures are generally laterally homogeneous because of turbulent mixing, while temperature contrasts occur primarily at tributary confluences, connected side channels, and oxbow lakes, where temperature acts as a tracer of hydrological connectivity and mixing. Thermokarst lakes across Arctic floodplains also exhibit strong spatial variability in surface temperature, likely reflecting differences in mixing and overturn processes, highlighting the need for spatially resolved thermal observations beyond point measurements. Overall, we demonstrate that remote sensing of surface water temperature provides substantially greater insight into the thermal structure and hydrological connectivity of Arctic river–wetland systems than is possible from existing gauge networks alone, and that these datasets can help advance understanding of the biological, geological, and biogeochemical processes shaping rapidly changing Arctic environments.

Acknowledgments

We thank J. Anadu, R. Blankenship, M. Douglas, K. Dunne, W. Fischer, E. Geyman, Y. Ke, H. Dion-Kirschner, J. Magyar, E. Mutter, J. Nghiem, J. Reahl, R. Rugama-Montenegro, E. Seelen, I. Smith and J. West for acquiring field data and for valuable discussions. We thank the Huslia Tribal Council for river and land access for the field team and S. Huffman and the Yukon River Inter-Tribal Watershed Council for field and logistical support. This material is based upon work supported by the National Science Foundation Graduate Research Fellowship under Grant No. 2139433 as well as by NSF Award 2031532 and Caltech's Resnick Sustainability Institute.

Open Research

The Landsat visible–near-infrared images and the Landsat Land Surface Temperature data are freely available from the United States Geological Survey/NASA through data portals such as EarthExplorer (https://earthexplorer.usgs.gov/). The stream gauge temperature data used in Figure 3 and the stream gauge discharge data used in Figs. 4, 8, and 10 are available from the United States Geological Survey National Water Information System (https://waterdata.usgs.gov/nwis). The near-surface air temperature data used in Figs. 4, 8, and 10 are available from the National Weather Service/Federal Aviation Administration/Department of Defense through data portals such as the National Centers for Environmental Information (https://www.ncei.noaa.gov/access/search/data-search/global-hourly). The in situ water temperature measurements of the Koyukuk River near Huslia, AK that were used in Figure 7 were taken by our collaborators. These data have been submitted for publication to the NSF Arctic Data Center and will be publicly available as soon as possible.

References

Åberg, J., Jansson, M., Karlsson, J., Nääs, K., & Jonsson, A. (2007). Pelagic and benthic net production of dissolved inorganic carbon in an unproductive subarctic lake. *Freshwater Biology*, *52*(3), 549–560. https://doi.org/10.1111/j.1365-2427.2007.01725.x

Alcântara, E. H., Stech, J. L., Lorenzzetti, J. A., Bonnet, M. P., Casamitjana, X., Assireu, A. T., & Novo, E. M. L. D. M. (2010). Remote sensing of water surface temperature and heat flux over a tropical hydroelectric reservoir. *Remote Sensing of Environment*, *114*(11), 2651–2665. https://doi.org/10.1016/j.rse.2010.06.002

Al-Murib, M. D., Wells, S. A., & Talke, S. A. (2019). Integrating Landsat TM/ETM+ and Numerical Modeling to Estimate Water Temperature in the Tigris River under Future

Climate and Management Scenarios. *Water*, *11*(5), 892. https://doi.org/10.3390/w11050892

Barsi, J., Schott, J., Hook, S., Raqueno, N., Markham, B., & Radocinski, R. (2014). Landsat-8 Thermal Infrared Sensor (TIRS) Vicarious Radiometric Calibration. *Remote Sensing*, *6*(11), 11607–11626. https://doi.org/10.3390/rs61111607

Baughman, C. A., & Conaway, J. S. (2021). Comparison of Historical Water Temperature Measurements with Landsat Analysis Ready Data Provisional Surface Temperature Estimates for the Yukon River in Alaska. *Remote Sensing*, *13*(12), 2394. https://doi.org/10.3390/rs13122394

Biela, V. R., Sergeant, C. J., Carey, M. P., Liller, Z., Russell, C., Quinn-Davidson, S., Rand, P. S., Westley, P. A. H., & Zimmerman, C. E. (2022). Premature Mortality Observations among Alaska's Pacific Salmon During Record Heat and Drought in 2019. *Fisheries*, *47*(4), 157–168. https://doi.org/10.1002/fsh.10705

Bilby, R. E. (1984). Characteristics and Frequency of Cool-water Areas in a Western Washington Stream. *Journal of Freshwater Ecology*, *2*(6), 593–602. https://doi.org/10.1080/02705060.1984.9664642

Boehrer, B., & Schultze, M. (2008). Stratification of lakes. *Reviews of Geophysics*, *46*(2), 2006RG000210. https://doi.org/10.1029/2006RG000210

Brabets, T.P. & Ourso, R.T. (2013). Water quality of streams draining abandoned and reclaimed mined lands in the Kantishna Hills area, Denali National Park and Preserve, Alaska, 2008–11. *Scientific Investigations Report 2013-5048*. https://doi.org/10.3133/sir20135048

Burn, C. R., & Kokelj, S. V. (2009). The environment and permafrost of the Mackenzie Delta area. *Permafrost and Periglacial Processes*, *20*(2), 83–105. https://doi.org/10.1002/ppp.655

Cannon, D. J., Troy, C. D., Liao, Q., & Bootsma, H. A. (2019). Ice-Free Radiative Convection Drives Spring Mixing in a Large Lake. *Geophysical Research Letters*, *46*(12), 6811–6820. https://doi.org/10.1029/2019GL082916

Chang, S. Y., Schwenk, J., & Solander, K. C. (2025). Deep Learning Advances Arctic River Water Temperature Predictions. *Water Resources Research*, *61*(6), e2024WR039053. https://doi.org/10.1029/2024WR039053

Chikita, K. A., Kemnitz, R., & Kumai, R. (2002). Characteristics of sediment discharge in the subarctic Yukon River, Alaska. *CATENA*, *48*(4), 235–253. https://doi.org/10.1016/S0341-8162(02)00032-2

Cole, J. J., Caraco, N. F., Kling, G. W., & Kratz, T. K. (1994). Carbon Dioxide Supersaturation in the Surface Waters of Lakes. *Science*, *265*(5178), 1568–1570. https://doi.org/10.1126/science.265.5178.1568

Cook, M., Schott, J., Mandel, J., & Raqueno, N. (2014). Development of an Operational Calibration Methodology for the Landsat Thermal Data Archive and Initial Testing of the Atmospheric Compensation Component of a Land Surface Temperature (LST) Product from the Archive. *Remote Sensing*, *6*(11), 11244–11266. https://doi.org/10.3390/rs61111244

Costard, F., Dupeyrat, L., Gautier, E., & Carey-Gailhardis, E. (2003). Fluvial thermal erosion investigations along a rapidly eroding river bank: application to the Lena River (central Siberia). *Earth Surface Processes and Landforms*, *28*(12), 1349–1359. https://doi.org/10.1002/esp.592

Das, N., Bhattacharjee, R., Choubey, A., Agnihotri, A. K., Ohri, A., & Gaur, S. (2022). Analysis of the Spatio-Temporal Variation of the Thermal Pattern of River Ganges in Proximity to Varanasi, India. *Journal of the Indian Society of Remote Sensing*, *50*(6), 1119–1134. https://doi.org/10.1007/s12524-022-01514-x

Donlon, C. J., Minnett, P. J., Gentemann, C., Nightingale, T. J., Barton, I. J., Ward, B., & Murray, M. J. (2002). Toward Improved Validation of Satellite Sea Surface Skin Temperature Measurements for Climate Research. *Journal of Climate*, *15*(4), 353–369. https://doi.org/10.1175/1520-0442(2002)015%253C0353:TIVOSS%253E2.0.CO;2

Douglas, M. M., Li, G. K., Fischer, W. W., Rowland, J. C., Kemeny, P. C., West, A. J., Schwenk, J., Piliouras, A. P., Chadwick, A. J., & Lamb, M. P. (2022). Organic carbon burial by river meandering partially offsets bank erosion carbon fluxes in a discontinuous permafrost floodplain. *Earth Surface Dynamics*, *10*(3), 421–435. https://doi.org/10.5194/esurf-10-421-2022

Douglas, M. M., Miller, K. L., Schmeer, M. N., & Lamb, M. P. (2023). Ablation-Limited Erosion Rates of Permafrost Riverbanks. *Journal of Geophysical Research: Earth Surface*, *128*(8), e2023JF007098. https://doi.org/10.1029/2023JF007098

Ebersole, J. L., Liss, W. J., & Frissell, C. A. (2003). Thermal heterogeneity, stream channel morphology, and salmonid abundance in northeastern Oregon streams. *Canadian Journal of Fisheries and Aquatic Sciences*, *60*(10), 1266–1280. https://doi.org/10.1139/f03-107

Eliason, E. J., Clark, T. D., Hague, M. J., Hanson, L. M., Gallagher, Z. S., Jeffries, K. M., Gale, M. K., Patterson, D. A., Hinch, S. G., & Farrell, A. P. (2011). Differences in Thermal Tolerance Among Sockeye Salmon Populations. *Science*, *332*(6025), 109–112. https://doi.org/10.1126/science.1199158

Earth Resources Observation and Science (EROS) Center. (2020). Landsat 8-9 Operational Land Imager / Thermal Infrared Sensor Level-2, Collection 2 [dataset]. U.S. Geological Survey. https://doi.org/10.5066/P9OGBGM6.

Farquharson, L. M., Mann, D. H., Grosse, G., Jones, B. M., & Romanovsky, V. E. (2016). Spatial distribution of thermokarst terrain in Arctic Alaska. *Geomorphology*, *273*, 116–133. https://doi.org/10.1016/j.geomorph.2016.08.007

Ford, D. J., Shutler, J. D., Blanco-Sacristán, J., Corrigan, S., Bell, T. G., Yang, M., Kitidis, V., Nightingale, P. D., Brown, I., Wimmer, W., Woolf, D. K., Casal, T., Donlon, C., Tilstone, G. H., & Ashton, I. (2024). Enhanced ocean CO2 uptake due to near-surface temperature gradients. *Nature Geoscience*, *17*(11), 1135–1140. https://doi.org/10.1038/s41561-024-01570-7

Franca, M. J., & Brocchini, M. (2015). Turbulence in Rivers. In P. Rowiński & A. Radecki-Pawlik (Eds.), *Rivers – Physical, Fluvial and Environmental Processes* (pp. 51–78). Springer International Publishing. https://doi.org/10.1007/978-3-319-17719-9_2

Frechette, D. M., Dugdale, S. J., Dodson, J. J., & Bergeron, N. E. (2018). Understanding summertime thermal refuge use by adult Atlantic salmon using remote sensing, river temperature monitoring, and acoustic telemetry. *Canadian Journal of Fisheries and Aquatic Sciences*, *75*(11), 1999–2010. https://doi.org/10.1139/cjfas-2017-0422

Geyman, E. C., Douglas, M. M., Avouac, J.-P., & Lamb, M. P. (2024). Permafrost slows Arctic riverbank erosion. *Nature*, *634*(8033), 359–365. https://doi.org/10.1038/s41586-024-07978-w

Gorham, E., & Boyce, F. M. (1989). Influence of Lake Surface Area and Depth Upon Thermal Stratification and the Depth of the Summer Thermocline. *Journal of Great Lakes Research*, *15*(2), 233–245. https://doi.org/10.1016/S0380-1330(89)71479-9

Grosse, G., Jones, B., & Arp, C. (2013). 8.21 Thermokarst Lakes, Drainage, and Drained Basins. In *Treatise on Geomorphology* (pp. 325–353). Elsevier. https://doi.org/10.1016/B978-0-12-374739-6.00216-5

Handcock, R. N., Torgersen, C. E., Cherkauer, K. A., Gillespie, A. R., Tockner, K., Faux, R. N., & Tan, J. (2012). Thermal Infrared Remote Sensing of Water Temperature in Riverine Landscapes. In P. E. Carbonneau & H. Piégay (Eds.), *Fluvial Remote Sensing for Science and Management* (1st ed., pp. 85–113). Wiley. https://doi.org/10.1002/9781119940791.ch5

Hossain, A. K. M. A., Mathias, C., & Blanton, R. (2021). Remote Sensing of Turbidity in the Tennessee River Using Landsat 8 Satellite. *Remote Sensing*, *13*(18), 3785. https://doi.org/10.3390/rs13183785

Hulley, G. C., Hughes, C. G., & Hook, S. J. (2012). Quantifying uncertainties in land surface temperature and emissivity retrievals from ASTER and MODIS thermal infrared data. *Journal of Geophysical Research: Atmospheres*, *117*(D23). https://doi.org/10.1029/2012JD018506

Isaak, D. J., Wollrab, S., Horan, D., & Chandler, G. (2012). Climate change effects on stream and river temperatures across the northwest U.S. from 1980–2009 and implications for salmonid fishes. *Climatic Change*, *113*(2), 499–524. https://doi.org/10.1007/s10584-011-0326-z

Jacob, C., McDaniels, T., & Hinch, S. (2010). Indigenous culture and adaptation to climate change: sockeye salmon and the St'át'imc people. *Mitigation and Adaptation Strategies for Global Change*, *15*(8), 859–876. https://doi.org/10.1007/s11027-010-9244-z

Javaheri, A., Babbar-Sebens, M., & Miller, R. N. (2016). From skin to bulk: An adjustment technique for assimilation of satellite-derived temperature observations in numerical models of small inland water bodies. *Advances in Water Resources*, *92*, 284–298. https://doi.org/10.1016/j.advwatres.2016.03.012

Kachari, J., Bhattacharjee, R., Piegay, H., Gaur, S., Ohri, A., & Kumar, R. (2024). The Spatial-Temporal Insights Into the Water Surface Temperature of the Kannauj-Patna Stretch of the River Ganga: A Remote Sensing Perspective. *2024 IEEE India Geoscience and Remote Sensing Symposium (InGARSS)*, 1–4. https://doi.org/10.1109/InGARSS61818.2024.10984274

Kaushal, S. S., Likens, G. E., Jaworski, N. A., Pace, M. L., Sides, A. M., Seekell, D., Belt, K. T., Secor, D. H., & Wingate, R. L. (2010). Rising stream and river temperatures in the United States. *Frontiers in Ecology and the Environment*, *8*(9), 461–466. https://doi.org/10.1890/090037

Kenworthy, S. T., & Rhoads, B. L. (1995). Hydrologic control of spatial patterns of suspended sediment concentration at a stream confluence. *Journal of Hydrology*, *168*(1–4), 251–263. https://doi.org/10.1016/0022-1694(94)02644-Q

Konsoer, K. M., & Rhoads, B. L. (2014). Spatial–temporal structure of mixing interface turbulence at two large river confluences. *Environmental Fluid Mechanics*, *14*(5), 1043–1070. https://doi.org/10.1007/s10652-013-9304-5

Kosten, S., Roland, F., Da Motta Marques, D. M. L., Van Nes, E. H., Mazzeo, N., Sternberg, L. D. S. L., Scheffer, M., & Cole, J. J. (2010). Climate-dependent CO_2 emissions from lakes. *Global Biogeochemical Cycles*, *24*(2). https://doi.org/10.1029/2009GB003618

Krabbenhoft, C. A., Allen, G. H., Lin, P., Godsey, S. E., Allen, D. C., Burrows, R. M., DelVecchia, A. G., Fritz, K. M., Shanafield, M., Burgin, A. J., Zimmer, M. A., Datry, T., Dodds, W. K., Jones, C. N., Mims, M. C., Franklin, C., Hammond, J. C., Zipper, S., Ward, A. S., … Olden, J. D. (2022). Assessing placement bias of the global river gauge network. *Nature Sustainability*, *5*(7), 586–592. https://doi.org/10.1038/s41893-022-00873-0

Layden, A., Merchant, C., & MacCallum, S. (2015). Global climatology of surface water temperatures of large lakes by remote sensing. *International Journal of Climatology*, *35*(15), 4464–4479. https://doi.org/10.1002/joc.4299

Ling, F., Foody, G., Du, H., Ban, X., Li, X., Zhang, Y., & Du, Y. (2017). Monitoring Thermal Pollution in Rivers Downstream of Dams with Landsat ETM+ Thermal Infrared Images. *Remote Sensing*, *9*(11), 1175. https://doi.org/10.3390/rs9111175

Lininger, K. B., & Wohl, E. (2019). Floodplain dynamics in North American permafrost regions under a warming climate and implications for organic carbon stocks: A review and synthesis. *Earth-Science Reviews*, *193*, 24–44. https://doi.org/10.1016/j.earscirev.2019.02.024

Miner, K. R., D'Andrilli, J., Mackelprang, R., Edwards, A., Malaska, M. J., Waldrop, M. P., & Miller, C. E. (2021). Emergent biogeochemical risks from Arctic permafrost degradation. *Nature Climate Change*, *11*(10), 809–819. https://doi.org/10.1038/s41558-021-01162-y

Minnett, P. J., Alvera-Azcárate, A., Chin, T. M., Corlett, G. K., Gentemann, C. L., Karagali, I., Li, X., Marsouin, A., Marullo, S., Maturi, E., Santoleri, R., Saux Picart, S., Steele, M., & Vazquez-Cuervo, J. (2019). Half a century of satellite remote sensing of sea-surface temperature. *Remote Sensing of Environment*, *233*, 111366. https://doi.org/10.1016/j.rse.2019.111366

Minnett, P. J., Smith, M., & Ward, B. (2011). Measurements of the oceanic thermal skin effect. *Deep Sea Research Part II: Topical Studies in Oceanography*, *58*(6), 861–868. https://doi.org/10.1016/j.dsr2.2010.10.024

Muñoz-Sabater, J., Dutra, E., Agustí-Panareda, A., Albergel, C., Arduini, G., Balsamo, G., Boussetta, S., Choulga, M., Harrigan, S., Hersbach, H., Martens, B., Miralles, D. G., Piles, M., Rodríguez-Fernández, N. J., Zsoter, E., Buontempo, C., & Thépaut, J.-N. (2021). ERA5-Land: A state-of-the-art global reanalysis dataset for land applications. *Earth System Science Data*, *13*(9), 4349–4383. https://doi.org/10.5194/essd-13-4349-2021

Murphy, R. D., Hagan, J. A., Harris, B. P., Sethi, S. A., Smeltz, T. S., & Restrepo, F. (2021). Can Landsat Thermal Imagery and Environmental Data Accurately Estimate Water Temperatures in Small Streams? *Journal of Fish and Wildlife Management*, *12*(1), 12–26. https://doi.org/10.3996/JFWM-20-048

Piccolroaz, S., Zhu, S., Ladwig, R., Carrea, L., Oliver, S., Piotrowski, A. P., Ptak, M., Shinohara, R., Sojka, M., Woolway, R. I., & Zhu, D. Z. (2024). Lake Water Temperature Modeling in an Era of Climate Change: Data Sources, Models, and Future Prospects. *Reviews of Geophysics*, *62*(1), e2023RG000816. https://doi.org/10.1029/2023RG000816

Pöschke, F., Lewandowski, J., Engelhardt, C., Preuß, K., Oczipka, M., Ruhtz, T., & Kirillin, G. (2015). Upwelling of deep water during thermal stratification onset—A major mechanism of vertical transport in small temperate lakes in spring? *Water Resources Research*, *51*(12), 9612–9627. https://doi.org/10.1002/2015WR017579

Post, E., Alley, R. B., Christensen, T. R., Macias-Fauria, M., Forbes, B. C., Gooseff, M. N., Iler, A., Kerby, J. T., Laidre, K. L., Mann, M. E., Olofsson, J., Stroeve, J. C., Ulmer, F., Virginia, R. A., & Wang, M. (2019). The polar regions in a 2°C warmer world. *Science Advances*, *5*(12), eaaw9883. https://doi.org/10.1126/sciadv.aaw9883

Pouchoulin, S., Le Coz, J., Mignot, E., Gond, L., & Riviere, N. (2020). Predicting Transverse Mixing Efficiency Downstream of a River Confluence. *Water Resources Research*, *56*(10). https://doi.org/10.1029/2019WR026367

Prabhakara, C., Dalu, G., & Kunde, V. G. (1974). Estimation of sea surface temperature from remote sensing in the 11- to 13-μm window region. *Journal of Geophysical Research*, *79*(33), 5039–5044. https://doi.org/10.1029/JC079i033p05039

Romanovsky, V. E., Smith, S. L., & Christiansen, H. H. (2010). Permafrost thermal state in the polar Northern Hemisphere during the international polar year 2007–2009: A synthesis. *Permafrost and Periglacial Processes*, *21*(2), 106–116. https://doi.org/10.1002/ppp.689

Santos Fleischmann, A., Papa, F., Hamilton, S. K., Melack, J., Forsberg, B., Val, A., Collischonn, W., Laipelt, L., Brusso Rossi, J., Comini De Andrade, B., Mendel, B., Alves, P., Bandeira, M., Custódio, Lady, Gomes, M. C., Hymans, D., Keppe, I., Mendes, R., Nascimento, R., … Marmontel, M. (2025). Extreme warming of Amazon waters in a changing climate. *Science*, *390*(6773), 606–611. https://doi.org/10.1126/science.adr4029

Schluessel, P., Emery, W. J., Grassl, H., & Mammen, T. (1990). On the bulk-skin temperature difference and its impact on satellite remote sensing of sea surface temperature. *Journal of Geophysical Research: Oceans*, *95*(C8), 13341–13356. https://doi.org/10.1029/JC095iC08p13341

Serikova, S., Pokrovsky, O. S., Laudon, H., Krickov, I. V., Lim, A. G., Manasypov, R. M., & Karlsson, J. (2019). High carbon emissions from thermokarst lakes of Western Siberia. *Nature Communications*, *10*(1), 1552. https://doi.org/10.1038/s41467-019-09592-1

Shi, X., Sun, J., & Xiao, Z. (2021). Investigation on River Thermal Regime under Dam Influence by Integrating Remote Sensing and Water Temperature Model. *Water*, *13*(2), 133. https://doi.org/10.3390/w13020133

Smith, L. C., Sheng, Y., MacDonald, G. M., & Hinzman, L. D. (2005). Disappearing Arctic Lakes. *Science*, *308*(5727), 1429–1429. https://doi.org/10.1126/science.1108142

Smith, M. I., Ke, Y., Geyman, E. C., Reahl, J. N., Douglas, M. M., Seelen, E. A., Magyar, J. S., Dunne, K. B. J., Mutter, E. A., Fischer, W. W., Lamb, M. P., & West, A. J. (2024). Mercury stocks in discontinuous permafrost and their mobilization by river migration in the Yukon River Basin. *Environmental Research Letters*, *19*(8), 084041. https://doi.org/10.1088/1748-9326/ad536e

Sobek, S., Tranvik, L. J., & Cole, J. J. (2005). Temperature independence of carbon dioxide supersaturation in global lakes. *Global Biogeochemical Cycles*, *19*(2). https://doi.org/10.1029/2004GB002264

Striegl, R. G., Dornblaser, M. M., McDonald, C. P., Rover, J. A., & Stets, E. G. (2012). Carbon dioxide and methane emissions from the Yukon River system. *Global Biogeochemical Cycles*, *26*(4). https://doi.org/10.1029/2012GB004306

Taranu, Z. E., Köster, D., Hall, R. I., Charette, T., Forrest, F., Cwynar, L. C., & Gregory-Eaves, I. (2010). Contrasting responses of dimictic and polymictic lakes to environmental change: A spatial and temporal study. *Aquatic Sciences*, *72*(1), 97–115. https://doi.org/10.1007/s00027-009-0120-4

Thorstad, E. B., Bliss, D., Breau, C., Damon-Randall, K., Sundt-Hansen, L. E., Hatfield, E. M. C., Horsburgh, G., Hansen, H., Maoiléidigh, N. Ó., Sheehan, T., & Sutton, S. G. (2021). Atlantic salmon in a rapidly changing environment—Facing the challenges of reduced marine survival and climate change. *Aquatic Conservation: Marine and Freshwater Ecosystems*, *31*(9), 2654–2665. https://doi.org/10.1002/aqc.3624

Torgersen, C. E., Faux, R. N., McIntosh, B. A., Poage, N. J., & Norton, D. J. (2001). Airborne thermal remote sensing for water temperature assessment in rivers and streams. *Remote Sensing of Environment*, *76*(3), 386–398. https://doi.org/10.1016/S0034-4257(01)00186-9

Torgersen, C. E., Baxter, C. V., Ebersole, J. L., & Gresswell, R. E. (2012). Incorporating Spatial Context into the Analysis of Salmonid–Habitat Relations. In M. Church, P. M. Biron, & A. G. Roy (Eds.), *Gravel-Bed Rivers* (1st ed., pp. 216–224). Hoboken, NJ: Wiley. https://doi.org/10.1002/9781119952497.ch18

USGS (2025). *Landsat 8-9 Calibration and Validation (Cal/Val) Algorithm Description Document (ADD).* (Version 5.0).

Vermote, E., Roger, J. C., Franch, B., & Skakun, S. (2018). LaSRC (Land Surface Reflectance Code): Overview, application and validation using MODIS, VIIRS, LANDSAT and Sentinel 2 data's. *IGARSS 2018 - 2018 IEEE International Geoscience and Remote Sensing Symposium*, 8173–8176. https://doi.org/10.1109/IGARSS.2018.8517622

Villamizar, S. R., Pai, H., Butler, C. A., & Harmon, T. C. (2014). Transverse spatiotemporal variability of lowland river properties and effects on metabolic rate estimates. *Water Resources Research*, *50*(1), 482–493. https://doi.org/10.1002/2013WR014245

Wang, Y., Deng, Y., Yang, Y., Tuo, Y., Wang, X., & Zhu, J. (2025). Investigation of the Spatiotemporal Patterns in Water Surface Temperature from Landsat Data in Plateau Rivers. *Remote Sensing*, *17*(7), 1141. https://doi.org/10.3390/rs17071141

Wawrzyniak, V., Piégay, H., & Poirel, A. (2012). Longitudinal and temporal thermal patterns of the French Rhône River using Landsat ETM+ thermal infrared images. *Aquatic Sciences*, *74*(3), 405–414. https://doi.org/10.1007/s00027-011-0235-2

Wawrzyniak, V., Piégay, H., Allemand, P., Vaudor, L., & Grandjean, P. (2013). Prediction of water temperature heterogeneity of braided rivers using very high resolution thermal infrared (TIR) images. *International Journal of Remote Sensing*, *34*(13), 4812–4831. https://doi.org/10.1080/01431161.2013.782113

Wei, J.-A., Wang, D., Gong, F., He, X., & Bai, Y. (2017). The Influence of Increasing Water Turbidity on Sea Surface Emissivity. *IEEE Transactions on Geoscience and Remote Sensing*, *55*(6), 3501–3515. https://doi.org/10.1109/TGRS.2017.2675623

Wen-Yao, L., Field, R. T., Gantt, R. G., & Klemas, V. (1987). Measurement of the surface emissivity of turbid waters. *Remote Sensing of Environment*, *21*(1), 97–109. https://doi.org/10.1016/0034-4257(87)90009-5

Westley, P. A. H. (2020). Documentation of *en route* mortality of summer chum salmon in the Koyukuk River, Alaska and its potential linkage to the heatwave of 2019. *Ecology and Evolution*, *10*(19), 10296–10304. https://doi.org/10.1002/ece3.6751

Wilson, R. C., Hook, S. J., Schneider, P., & Schladow, S. G. (2013). Skin and bulk temperature difference at Lake Tahoe: A case study on lake skin effect. *Journal of Geophysical Research: Atmospheres*, *118*(18). https://doi.org/10.1002/jgrd.50786

Wrzesiński, D., & Graf, R. (2022). Temporal and spatial patterns of the river flow and water temperature relations in Poland. *Journal of Hydrology and Hydromechanics*, *70*(1), 12–29. https://doi.org/10.2478/johh-2021-0033

Wu, J.-L., Ho, C.-R., Huang, C.-C., Srivastav, A., Tzeng, J.-H., & Lin, Y.-T. (2014). Hyperspectral Sensing for Turbid Water Quality Monitoring in Freshwater Rivers:

Empirical Relationship between Reflectance and Turbidity and Total Solids. *Sensors*, *14*(12), 22670–22688. https://doi.org/10.3390/s141222670

Zabelina, S. A., Shirokova, L. S., Klimov, S. I., Chupakov, A. V., Lim, A. G., Polishchuk, Y. M., Polishchuk, V. Y., Bogdanov, A. N., Muratov, I. N., Guerin, F., Karlsson, J., & Pokrovsky, O. S. (2021). Carbon emission from thermokarst lakes in NE European tundra. *Limnology and Oceanography*, *66*(S1). https://doi.org/10.1002/lno.11560

Zandt, M. H., Frank, J., Yilmaz, P., Cremers, G., Jetten, M. S. M., & Welte, C. U. (2020). Long-term enriched methanogenic communities from thermokarst lake sediments show species-specific responses to warming. *FEMS Microbes*, *1*(1), xtaa008. https://doi.org/10.1093/femsmc/xtaa008

Zou, Z., Xiao, X., Dong, J., Qin, Y., Doughty, R. B., Menarguez, M. A., Zhang, G., & Wang, J. (2018). Divergent trends of open-surface water body area in the contiguous United States from 1984 to 2016. *Proceedings of the National Academy of Sciences*, *115*(15), 3810–3815. https://doi.org/10.1073/pnas.1719275115